MSc thesis
Universiteit Utrecht; Georgia Institute of Technology
Supervisors: Prof.dr. C.J. Spiers, Dr. C.J. Peach, Dr. C.F. Arson
Utrecht, September 2015

The effect of evolving grain contact and pore wall area on compaction creep of granular NaCl by pressure solution

Douma, L.A.N.R.[1]

[1]Faculty of Geosciences, Universiteit Utrecht, L.A.N.R.Douma@students.uu.nl

Abstract

It is widely accepted that inter granular pressure solution is a dominant deformation mechanism in solid/liquid systems. However, several authors suggest that this stress driven mechanism slows down, where opposing interfacial energy driving forces become important, and will stop until a certain 'yield stress' for pressure solution is reached, below which the process is prevented by surface energy grain boundary healing. This yield stress for rock salt and dominant mechanism(s) operating when pressure solution creep slows down and even stops has received little attention.

In this research, short term uniaxial compaction experiments were conducted under chemically closed system conditions on brine- and n-decane saturated granular salt to allow identification of the compaction mechanism(s) and to test the applicability of the predictions made by accepted analytical pressure solution models. In combination with long term compaction experiments and microstructural observations, the mechanisms operating and associated interfacial surface energies in low and high strain fields were defined. It is found that the experimental data on brine-saturated granular salt follows the analytical models of diffusion controlled pressure solution until volumetric strains up to 20%, whereas the addition of n-decane counteracts on dissolution and precipitation processes can not operate. Microsctructural observations confirm that pressure solution creep was the dominant deformation mechanism at low volumetric strains (<15%) (i.e. high porosities) and neck growth and grain boundary migration were deformation mechanisms operating at high volumetric strains (>20%) (i.e. low porosities). A yield stress of 55 MPa was found, indicating that grain boundary healing occurred and pressure solution slows down and eventually stops at high volumetric strains (32%). The grain contact area turned out to be larger than pore wall area at low porosities, whereas the grain contact area < pore wall area when pressure solution creep operates.

Contents

1 Introduction

Rock salt has long been recognized as a highly suitable medium for geological storage of oil and gas, because salt can heal itself by plastic flow and diffusive mass transfer, has a low permeability, low creep strength and is highly ductile (Koelemeijer et al. (2012); Popp et al. (2012); Zhu and Arson (2014a)). Besides oil and gas, underground salt mines can be used for long-term nuclear-waste storage and for storage of energy in the form of compressed air for buffering wind, solar and tidal energy supplies (Koelemeijer et al. (2012); Zhu and Arson (2014a); Zhu and Arson (2014b)). As well, rock salt overlying depleted oil or gas reservoirs offers a highly favorable cap rock for geological storage of CO_2 and is able to effectively seal the boreholes through the salt. In all the mentioned applications too, the favorable creep and healing characteristics and low gas permeability, make salt an attractive host rock for deep disposal.

Inter granular pressure solution is thought to be one of the important mechanisms of deformation in rock salt and operates when brine is present in the system (e.g., Spiers et al. (1990); Spiers and Schutjens (1999); van Noort et al. (2008); Pluymakers and Spiers (2014)) This time dependent deformation mechanism operates under relative low stresses and temperature conditions and is known to be important in fluid-rock aggregates where dislocation creep is low (Visser et al. (2012)) and is assisted by diffusive mass transfer of material along the grain boundaries in an island channel form (e.g. Spiers et al. (1990); Lehner (1995); Pluymakers and Spiers (2014)) or adsorbed film (e.g. Rutter and Elliott (1976),;Pluymakers and Spiers (2014)). Material will dissolve at the grain boundary interfaces due to the increase in solubility at the solid-solid contact under high mean normal stress, compared to the pore wall regions. The material is diffused through the grain boundary solvent phase and precipitate at the interfaces under low mean normal stress (pore wall areas) (e.g. Spiers et al. (1990); Zhang and Spiers (2005)) resulting in volumetric compaction, porosity and permeability reduction of granular material. It was found that pressure solution processes accelerate in fine grained materials (Meer and Spiers (1997); Zhang and Spiers (2005)), and are therefore of interest in relation to compaction, healing and sealing processes (Visser et al. (2012)). During this stress driven mechanism, interfacial energies were often assumed to be negligible. However, inter facial energy driven processes such as neck growth can result in grain boundary healing slowing down or eventually stop the process of pressure solution. For predictions on compaction and healing/sealing rates, it is important to know what determines the compaction/healing rate at low porosities in a solid-liquid NaCl system and how is it related to the contact and pore area. Does pressure solution still operate or is the system dominated by interfacial energy driven processes?

In this report, wet and dry uniaxial compaction experiments on granular salt were conducted in which the applied stress, grain size and fluid type were varied. The dependence on stress, grain size and fluid type could be determined and compared with diffusion controlled pressure solution models. In combination with microstructural observations, the mechanisms dominating for low volumetric strains (<15%) (i.e. high porosities ($\phi > 30\%$) and high volumetric strains (>15%) (i.e. low porosities ($\phi < 20\%$) were investigated. Microscopic image analysis was carried out to define porosity, grain size, pore size and contact size to characterize the regime. A possible 'yield stress' for pressure solution, the critical stress at which healing starts and pressure solution stops, was determined using the microstructural data and compared with models that predict the critical stress at which healing starts (van Noort et al. (2008)).

2 Theoretical background

In this section, two different mechanisms that are important for rock deformation were opposed. First of all, we introduce the behavior of solid-liquid systems under stress (pressure solution creep) and second the behavior of solid-liquid system during neck growth/healing. During pressure solution, the solubility at grain to grain contact increased compared to the pore-wall regions, whereby material is transported from contacts to pores, resulting in compaction of the aggregate and porosity reduction. Important for this mechanism to operate is that stress was applied to the system and a fluid was needed to penetrate in the grain boundaries. Neck growth, however, results in mass transfer from the pores towards the grain contacts (Visser (1999)). Note that no applied stress is necessary for neck growth to operate in a solid-liquid system. The interfacial energy seems to be the most important factor for neck growth to operate (Hickman and Evans (1991)).

2.1 Thermodynamic driving force for pressure solution creep

Figure 1 shows the model of diffusive mass transfer due to pressure solution creep. In this model we assume a closed system with equi-dimensional spherical grains. The grain boundaries contain fluids in the form of (1) a strongly adsorbed thin film or (2) in an island-channel network containing a fluid at uniform pressure (e.g. Spiers et al. (1990); Shimizu (1995)). For an adsorbed thin film, we assume that H_2O molecules are bonded onto the grain surfacesp producing a diffusivity path (Rutter and Elliott (1976)). The grain boundaries are not in equilibrium, because the contact points will dissolve and reform somewhere else (Pluymakers and Spiers (2014)). We assume that the fluid films of an island-channel network have a thickness of at least 25-250 nm and is filled with a fluid at uniform pressure (Pluymakers and Spiers (2014)). We assume that the shape of the grain boundary fluid does not influence the creep model for pressure solution (Pluymakers and Spiers (2014)). Many authors (e.g. Spiers et al. (1990); Lehner (1995); Shimizu (1995)) showed already that the thermodynamic

driving force for inter granular pressure solution in a closed system is maintained by the gradients in chemical potential and gradients in solubility of the solid (Spiers et al. (2003)). When rock salt is loaded and when a pore fluid is present, the stress-induced differences will enhance the solubility between the grain contacts that are under stress (indicated by 'a' in Fig. 1) and the free pore walls (indicated by 'b' in Fig. 1) and if the driving force for material to dissolve at the grain contacts and precipitate on the pore wall surfaces (e.g. Rutter and Elliott (1976); Raj (1982); Rutter (1983);Pluymakers and Spiers (2014)). The potential energy of the stressed solid that is in contact with a solution at the grain boundary (e.g. Rutter and Elliott (1976); Spiers et al. (1990); Lehner (1995); Shimizu (1995); Spiers et al. (2003)) can be written as

$$\mu_{gb} \approx f^s + \sigma_n \Omega \tag{1}$$

Where f^s is the Helmholtz fee energy of the solid, Ω the molar volume of the solid at the grain boundary zone and σ_n the compressive normal stress. At the pore wall sides, the chemical potential energy (e.g. Rutter and Elliott (1976); Spiers et al. (1990); Lehner (1995); Shimizu (1995); Spiers et al. (2003)) can be described by

$$\mu_{gb} \approx f^s + P_f \Omega \tag{2}$$

Where P_f is the pore fluid pressure. The solubility at the grain to grain contacts will increase compared to the pore wall regions when a stress is applied to the salt grain. The material will be transported from the contacts to the pores resulting in a drop in the normal component of the solid chemical potential ($\Delta\mu_n$) (Visser et al. (2012); Spiers et al. (1990); Meer and Spiers (1997); Zhang and Spiers (2005)). We can neglect the small gradients in f^s within the solid grains and the potential drop around the grain boundaries (Spiers et al. (2003)) can be written as

$$\Delta\mu_n = \Delta\sigma_n \Omega \tag{3}$$

The difference in potential energy in the pore wall area (Spiers et al. (2003)) can be written as

$$\Delta\mu_n = (\Delta\sigma_n - P_f)\Omega \tag{4}$$

Where μ_n is the normal component of solid chemical potential, σ_n is the mean normal stress acting on a given site. The standard relation for ideal mixtures between the chemical potential of the dissolved solid and its concentration (C) is expressed by

$$\mu = \mu_0 + RTln\frac{C}{C_0} \tag{5}$$

By using equation (5) the chemical potential drop can be written as a function that corresponds to the difference in solubility of the solid (ΔC) (Spiers et al. (2003))

$$\Delta\mu_n = RTln\frac{C_s + \Delta C}{C_s} \approx RT\frac{\Delta C}{C_0} \tag{6}$$

where R is the gas constant, T the absolute temperature, ΔC $[m^3/m^3]$ the enhancement of the solubility of the solid at the source site relative to the sink site and C_s $[m^3/m^3]$ is the solubility of the solid at the sink (Spiers et al. (1990)). The driving force $\Delta\mu_n$ during pressure solution acts over three processes, including dissolution (at points of high σ_n), diffusion through the grain boundary fluid phase and precipitation (at points of low σ_n). The creep is controlled by the kinetics of these reactions by

$$\Delta\mu_n = \Delta\mu_s + \Delta\mu_d + \Delta\mu_p \tag{7}$$

Where s, d, p denote to potential drop or driving force associated with the dissolution, diffusion and precipitation respectively (Spiers et al. (2003); Pluymakers and Spiers (2014)). The total work due to pressure solution creep is the sum of the the kinetic processes (i.e. dissolution, diffusion, precipitation). The rate of compaction is controlled by the process that forms the slowest overall step (Spiers et al. (1990)). Creep models are shown for the three potential processes that can control the rate. A relation between the rate of the process of dissolution, diffusion and precipitation and the stress dependent driving force ($\Delta\mu_n$) was established by several authors (e.g. Raj (1982); Lehner (1995)). For the interface controlled pressure solution creep (i.e. dissolution and precipitation controlled) we assume linear reaction rate equations that characterize crystal growth and dissolution. These can be written as

$$V_s = I_s\Delta\mu_n/RT = k_s\Omega\Delta\mu_n/RT \tag{8}$$

$$V_p = I_p\Delta\mu_n/RT = k_p\Omega\Delta\mu_n/RT \tag{9}$$

Where V_s and V_p represent the velocities of dissolution and precipitation $[ms^{-1}]$, I_s (and k_s) and I_p (and k_p) represent the reaction rate coefficients for dissolution and precipitation. If the pressure solution creep is diffusion controlled, the process rate is related to the Fickian diffusion flux in the grain boundary (Spiers et al. (1990)) and can be written as

$$J_{gb} = -(DC\Omega/RT) \bigtriangledown \mu_{gb} \tag{10}$$

Where D $[m^2s^{-1}]$ is the grain boundary diffusion coefficient, R the gas constant, T the absolute temperature and C the solubility of the solute in the grain boundary fluid $[m^3/m^3]$.

Numerous authors (e.g. Rutter and Elliott (1976); Raj (1982); Spiers et al. (1990)) derived theoretically rate conditions under closed conditions. These models lead to approximately the same results (Spiers et al. (2003)), but describe the influence of grain packing and porosity differently. The constitutive equations (i.e. when interfacial energy effects are negligible) for the three processes can basically written as

$$\dot{\varepsilon_s} = A_s \frac{I_s}{d} \frac{\sigma_e \Omega}{RT} f_s(\phi) \tag{11}$$

$$\dot{\varepsilon_d} = A_d \frac{(DCS)}{d^3} \frac{\sigma_e \Omega}{RT} f_d(\phi) \tag{12}$$

$$\dot{\varepsilon_p} = A_p \frac{I_p}{d} \frac{\sigma_e \Omega}{RT} f_p(\phi) \tag{13}$$

(Lehner (1995); Spiers et al. (2003); Meer and Spiers (1997)). The variables are defined in Table 1. Numerous authors (e.g. Lehner (1995); Spiers et al. (1990); Meer and Spiers (1997)) show that dissolution and precipitation are relatively fast in a NaCl-brine system. In the next subsection, the constitutive equations for diffusion controlled pressure solution are defined based on the constitutive model of (1) Spiers et al. (1990) and (2) Pluymakers and Spiers (2014). Both models assume a geometry of a simple cubic pack of equidimensional spherical grains, but describe the changes in grain contact area, transport path length and pore wall area during compaction differently (i.e. other description of A and $f_{s,d,p}(\phi)$).

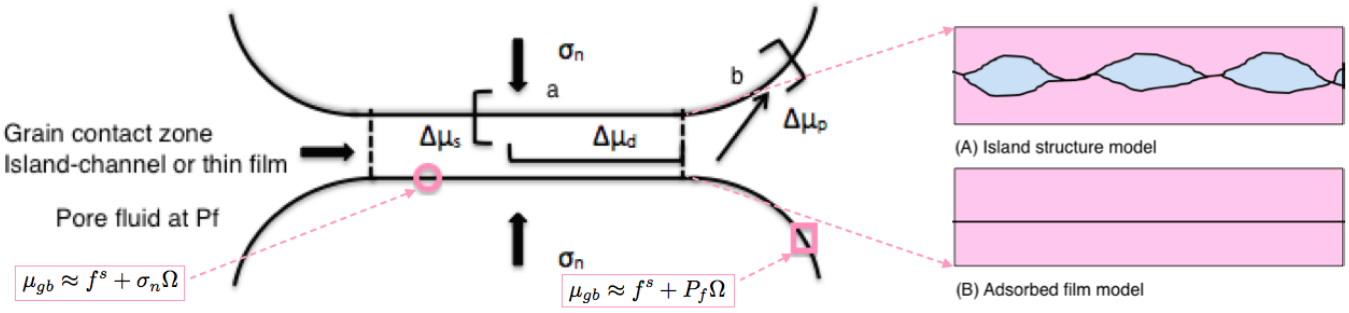

Figure 1: *Intergranular pressure solution creep under closed system. Dissolution of material is driven by the differences in chemical potential from the solid-solid contact to the solid-liquid interfaces, transported via the grain boundary ($\Delta\mu_d$) and precipitated at the free pore walls ($\Delta\mu_p$). σ_n indicates the mean normal stress and P_f the pore fluid pressure. Compaction and a decrease in porosity and permeability will be the result of pressure solution creep (Meer and Spiers (1997); Zhang and Spiers (2005)).*

2.2 Constitutive equations: diffusion controlled pressure solution creep

2.2.1 Model of Spiers et al. (1990) and parameters for NaCl

In the case of diffusion controlled compaction creep, the potential drop between the entire grain contact and the pore walls drives the grain boundary diffusion and $\Delta\mu_n = \Delta\mu_d$. For the case that diffusion is the rate controlling mechanism, the volumetric strain rate can be written as (Spiers et al. (1990))

$$\dot{\varepsilon_d} = AV_m \frac{Z^*}{T} \frac{\sigma_e^n}{d^3 e_v^a} \tag{14}$$

Where $\dot{\varepsilon_d}$ represents the volumetric strain rate, A are geometric constants, σ_e the applied effective axial stress, S the average thickness of the grain boundary fluid phase [m], d the grain size, e_v the volumetric strain. Note that e_v can be written as $e_v = \frac{\phi_0 - \phi}{1 - \phi_0}$ and is therefore a function of porosity ($f(\phi)$) that accounts for the changes in contact area, transport path length and pore wall area during compaction and describes the geometry of a regular spherical grain pack in the model of Spiers et al. (1990). So, if we relate this to Equation12 we can say

$$\dot{\varepsilon_d} = AV_m \frac{(DCS)}{d^3} \frac{\sigma_e \Omega}{RT} \left(\frac{1 - \phi_0}{\phi_0 - \phi} \right)^a \tag{15}$$

Z^* is the phenomenological coefficient and determines the absolute rate of creep (for both the adsorbed film as the island channel grain boundary model) and can be written as an Arrhenius dependence on temperature

$$Z^* = D_0 C_0 exp(-\Delta H/RT)S \tag{16}$$

DCS represents the grain boundary diffusivity (Z_0). We assume that these parameters that define Z^* are independent of the deformation geometry. Combining equation (14) and (15) will give the following temperature dependent diffusion controlled pressure solution creep model for porous aggregates

$$\dot{\varepsilon_d} = AV_m \frac{D_0 C_0 exp(-\Delta H/RT)}{T} \frac{\sigma_e}{d^3 e_v^a} \tag{17}$$

The compaction creep experiments presented in this report are related to the above mentioned compaction creep model to investigate the pressure solution phenomena and to determine the fundamental parameter Z^*.

2.2.2 Model of Pluymakers and Spiers (2014)

Geometrical model
The spherical model of Pluymakers and Spiers (2014) assumes an aggregate geometry that consist of a simple cubic pack of spheres of uniform size with flat grain contacts (Fig. 2). The function of porosity differs from the model of Spiers et al. (1990). A normal stress is applied on the salt grains (σ_n) and the pores are filled with pre saturated brine solution. A uniform pressure (P_f) acts on the pore walls. Pluymakers and Spiers (2014) describes the force balance as follows

$$\sigma_n a_c + P_f(d_c^2 - a_c) = P d_c^2 \tag{18}$$

Whereby $\sigma_n a_c$ indicates the force at the contacts, $P_f(d_c^2 - a_c)$ the force on the grain due to the pore fluid pressure and Pd_c^2 the applied force per grain. By rewriting equation (17) the normal stress on the contacts can be defined by

$$\sigma_n = (P - P_f)\frac{d_c^2}{a_c} + P_f \tag{19}$$

a_c represents the mean grain contact area and can be written as a function of porosity $f(\phi)$ by

$$a_c = \frac{Fd^2}{Z} f(\phi) \tag{20}$$

Where F is the shape factor value (π) and Z the grain coordination number. The simple function of porosity for the model of Pluymakers and Spiers (2014) is written as

$$f(\phi) = \frac{q - 2\phi}{q} \tag{21}$$

Where $q = 2\phi_0$. Note that equation (20) only count for porosities down *c.* 5%, because with ongoing solution can transform the grain geometry from a sphere to a cube (Schaap (1993); Pluymakers and Spiers (2014)). The function of porosity $f(\phi)$ describes the increase in grain contact area with decreasing ϕ in the relation

$$A_c = \pi d^2 f(\phi) \tag{22}$$

Where A_c denotes the grain contact area per grain (i.e. $6a_c$ for SC packing), πd^2 the total surface area (A_t) of the spherical grains with diameter d and $f(\phi)$ the fraction of the total grain surface A_t contributed by the contacts.The pore wall area per grain (A_{pw}) can be written as

$$A_{pw} = Fd^2 - A_c \tag{23}$$

Diffusion controlled pressure solution creep equations

The average potential difference between the solid and within the grain contact and at the pore walls can be written as $\Delta\mu_n = \Delta\mu d = (\sigma_n - P_f)\Omega \approx (Z/F)(\sigma_n^e\Omega)q/(q-2\phi)$ for the model of Pluymakers and Spiers (2014). The model presented by Pluymakers and Spiers (2014) for diffusion controlled pressure solution for porosity values between 40% and 5% can be written as

$$\dot{\varepsilon_{d1}} = \frac{2\pi A_c D C_s S Z}{\beta a_c} \left[exp(\frac{\sigma_n^e \Omega}{RT}\frac{Z}{F}\frac{q}{q-2\phi}) - 1 \right] \times \left(\frac{q}{q-2\phi}\right) \tag{24}$$

Where $C_s = C_0\Omega$ (m^3m^{-3}). When $(\sigma_n^e\Omega/RT)(Z/F)q/(q-2\phi)$ is small, this can be approximated as

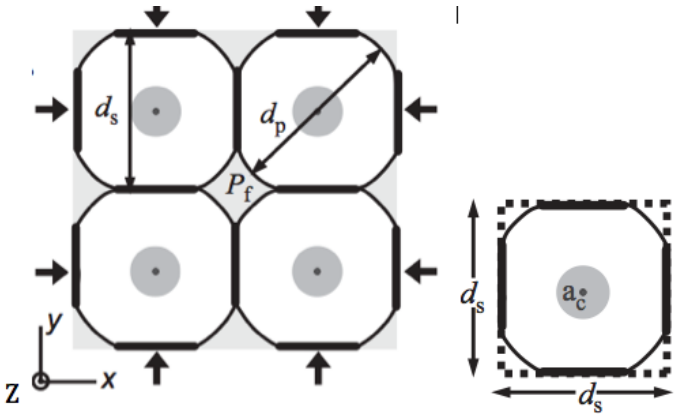

Figure 2: *Geometry of the grains as assumed in the compaction creep model of Pluymakers and Spiers (2014) for granular aggregates. The aggregate consist of a simple cubic pack of spheres, whereby the grain contacts are flat. The pores are filled with saturated solution and have a uniform pressure P_f*

$$\dot{\varepsilon_{d2}} = \frac{2\pi A_c D C_s S Z^2}{\beta F^2 d^3} \frac{\sigma_n^e \Omega}{RT} \left(\frac{q}{q - 2\phi} \right)^2 \tag{25}$$

The model for diffusion controlled pressure solution involves equating the mechanical work rate $\dot{W}$ $(Jm^{-3}s^{-1})$ to the rate of dissipation by grain boundary diffusion $\dot{\Delta}_d$ (Pluymakers and Spiers (2014)). The expression for diffusion controlled pressure solution in a more rigorous approach can be written as

$$\dot{\varepsilon_{d3}} = \frac{4\pi A_d Z}{F} \frac{D C_s S}{d^3} \frac{\sigma_n^e \Omega}{RT} \frac{Z}{F} \left(\frac{q}{q - 2\phi} \right)^2 \tag{26}$$

Where A_d is 6 for isotropic compaction and lies in the range 4 ± 2 for 1D strain.

Table 1: *Symbols and definitions used in equation 1-26*

Symbol	Definition	Units
A	Grain shape and packing factor divided by gas constant. For spherical grains, $A \approx 33$	$Mol.K.J^{-1}$
A_c	Grain contact area per grain	m^2
$A_{s,p,d}$	Geometric factor depending on packing plus deformation geometry	-
A_{pw}	Pore wall area per grain	m^2
a_c	Area of an individual grain contact	m^2
a	Numerical exponent. For $e_v = 3-10\%$ a=2; $e_v = 15-20\%$ a=4-5	-
β	Geometric factor accounting for diffusion distance	-
C_0	Solubility of dissolved solid in grain boundary fluid (unstressed case)	$molfraction$
C	Solubility of stressed material	$molfraction$
ΔC	Absolute enhancement in the solubility of the solid at stressed grain contacts	$molm^{-3}$
C_s	Local mean concentration of dissolved solid in grain boundary fluid	$molm^{-3}$
D_0	Diffusivity of dissolved solid in grain boundary fluid	$m^2.s^{-1}$
d	Grain size	m
d_s	Truncated diametral grain spacing	m
d_p	Grain diameter measured at pore wall	m
d, p, s	Subscripts indicating diffusion, precipitation or dissolution control respectively	-
$\dot{\varepsilon}_{s,d,p}$	Volumetric strain rate	s^{-1}
e_v	Volumetric strain $e_v = \frac{\Delta V}{V_0}$, where ΔV is the volume change and V_0 the initial volume	-
ϕ	Porosity	-
ϕ_0	Start porosity	-
f^s	Helmholtz free energy of the solid	J
F	Grain shape factor (π for spherical grains)	-
$\gamma_{sl/ss}$	Interfacial free energy (solid-liquid or solid-solid) respectively	
ΔH	Activation energy for grain boundary diffusion	$J.mol^{-1}$
I_s	Dissolution rate constant	$m.s^{-1}$
I_p	Precipitation rate constant	$m.s^{-1}$
L	Grain coordination number. For simple cubic pack: $L = 6$	-
μ_n	Chemical potential	J
μ_m	Chemical potential of the solid at the neck margin	J
μ_p	Chemical potential of the solid at the pore walls	J
$\Delta\mu_{d,p,s}$	Chemical potential drop associated with d-, p-, or s-controlled pressure solution	J
$\Delta\mu_n$	Drop in normal component of chemical potential	J
n	Constant: 1	-
Ω	Molar volume of solid phase	m^3mol^{-1}
P_f	Fluid pressure acting on free pore walls	MPa
P	Total applied hydrostatic stress	MPa
q	Geometric term equal to $2\phi_0$	-
R	Gas constant	$J.mol^{-1}.K^{-1}$
ρ	Radius of curvature	m
S	Thickness of the grain boundary fluid	m
σ_a	Applied stress	Pa
σ_n^e	Effective normal stress imposed on the aggregate	MPa
T	Absolute temperature	K
V_m	Molar volume of solid phase	$2.693.10^{-5}m^3$
$\dot{W}$	Mechanical work rate ($\sigma_n^e\dot{\varepsilon_s}$)	$Jm^{-3}s^{-1}$
x	Instantaneous neck radi	m
x_0	Initial neck radii	m
x_{cr}	Initial contact	m
Z^*	Phenomological coefficient	m^3s^{-1}
Z	Grain coordination number	-

2.3 Neck growth and healing

As mentioned before, pressure solution creep or solution/precipitation includes the process of densification under an applied effective stress and will result in mass transfer away from the grain contacts (Visser (1999)) (Fig. 3). Two other processes may occur at the grain boundary, namely (1) contact healing (van Noort et al. (2008)) and (2) neck growth at contact scale. When a stress is applied on the system, the islands might grow and result in contact healing. The mechanism of healing will stop the stress driven deformation mechanism (pressure solution creep) (Fig. 3), because the stress on the grain contacts decreases (i.e. contact area increases with ongoing deformation) and no mass transport from the contacts to the pores is possible.
Neck growth (i.e. growth of the grain contact by adding material to the grain margin), however, results in mass transfer from the pores towards the grain contacts (Visser (1999)). Atoms were transported through the fluid phase, from high chemical potential surface points to low chemical potential surface points. Interfacial energy seems the be the important driving force for neck growth to occur (Hickman and Evans (1991)), whereas the stress related driving forces are dominant for pressure solution creep. The dihedral angle is important for neck growth. For a curved surface, when there is at least one solid phase, the work required to create a unit area of a new surface at constant p, T and surface density differs from the surface tension (i.e. work done in the extending surface) (γ_{tens} (Visser (1999)). This means that changes in total interfacial energy were important. Due to the surface energy driving forces, the microstructure becomes in a equilibrium microstructure, meaning that an equilibrium microstructure was reached (Visser (1999)). The system is in equilibrium when

$$\gamma_{ss} = 2\gamma_{sl} cos(\frac{\theta_{eq}}{2}) \tag{27}$$

No neck growth will occur when the system is in equilibrium. When the dihedral angle (θ) $\neq$ equilibrium dihedral angel (θ_{eq}) neck growth can occur. When this angle $\neq$ the equilibrium angle, and the system is not driven by stress, neck growth can occur tending to 'stretch' the contacts (Fig. 3).

2.3.1 Equations: driving force for neck growth in a solid-liquid system (no stress applied)

Neck growth model Visser (1999)
The neck-growth model at contact scale presented by Visser (1999) assumed a start position representing a grain contact area and $\gamma_{ss} < \gamma_{sl}$ and no stress is applied on the system. Where γ_{ss} is the interfacial energy of the solid-solid and γ_{sl} the interfacial energy of the solid-liquid. We assume that the grain contacts were not penetrated by fluid The solid-solid and solid-liquid surfaces (A_{ss} and A_{sl} respectively) changed during the process of neck growth and will change therefore the internal energy of the system. The change of internal energy (u^{surf}) can be written as (Visser (1999)

$$u^{surf} = \gamma_{ss} A_{ss} + \gamma_{sl} A_{sl} \tag{28}$$

whereby the rate can be defined as

$$\dot{u} = \gamma_{ss} \frac{dA_{ss}}{dt} + \gamma_{sl} \frac{dA_{sl}}{dt} = 2\rho\dot{x} 2\phi x \frac{\Delta\mu}{\Omega^s} = 2\pi x\dot{x} 2\gamma_{sl}(cos\frac{\theta}{2} - cos\frac{\theta_{eq}}{2}) \tag{29}$$

Therefore, the change in chemical potential ($\Delta\mu$) van be written as

$$\frac{\gamma_{sl}}{\rho}\Omega^s(cos\frac{\Delta}{2} - cos\frac{\theta_{eq}}{2}) \tag{30}$$

As mentioned before, the rate controlling step depends on the slowest step: dissolution, diffusion and precipitation. For precipitation controlled neck-growth the velocity of precipitation can be written as

$$\dot{x} = \frac{2I^*\gamma_{sl}\Omega^s d}{kT}(cos\frac{\theta}{2} - cos\frac{\theta_{eq}}{2}) \tag{31}$$

When diffusion will control the neck growth rate, the equation can be written as

$$\dot{x} = \frac{4(DC)_{pore}}{\pi kT}\frac{\gamma_{sl}\Omega^s}{x^2}(cos\frac{\theta}{2} - cos\frac{\theta_{eq}}{2}) \tag{32}$$

The driving force ($\Delta\mu$) and rate equation ($\dot{x}$) for neck growth presented by Visser (1999) can be described by (respectively)

$$\Delta\mu \approx \frac{\gamma_{sl}\Omega^s}{\rho}(cos\frac{\theta}{2} - cos\frac{\theta_{eq}}{2}) \tag{33}$$

$$\dot{x} = A(T)R\gamma_{sl}(cos\frac{\theta}{2} - cos\frac{\theta_{eq}}{2})^a \frac{d^b}{(x^2 - x_{cr}^2)^c} \tag{34}$$

These models for neck growth without applying a stress show that the neck growth rates will increase when (1) γ_{sl}, (2) solubility and (3) diffusivity increases. The neck growth rates will decrease when the (1) neck diameter and (2) grain size increases and (3) the difference between the current and equilibrium dihedral angel decreases (Visser (1999)).

2.3.2 Equations: driving force for neck growth in a solid-liquid system under an applied stress.

Neck-growth model of van Noort et al. (2008)
This model assumes stressed grains with a island channel contact filled with a fluid. For a solid-fluid aggregate that deformed under a constant stress we can require

$$\gamma_{ss}\dot{A_{ss}} + \gamma_{sl}\dot{A_{sl}} + \Phi = \sigma_{ij}\dot{\epsilon}_{ij+P_f\dot{\phi}} + \Sigma\dot{\Delta}k \tag{35}$$

where γ_{ss} and γ_{sl} represents the solid-solid and solid-liquid interfacial energies respectively. A_{ss} and A_{sl} represent the rate of change in solid-solid and solid-liquidd interfacial areas ($m^{-1}s^{-1}$). Φ is the rate of change of free energy. When no deformation/compaction occurs and the system is hydrostatic, and $\theta_{eq} > 0$, the interfacial energy terms will drive neck growth from the pore wall regions toward the necks (van Noort et al. (2008)), whereby

$$\gamma_{ss}\dot{A}_{ss} + \gamma_{sl}\dot{A}_{sl} = D\dot{e}lta_{ng} \tag{36}$$

The driving force for the chemical potential drops that drives material from the pore wall to the contact margin and causes neckgrowth can be written as

$$\Delta\mu = \frac{\gamma_{sl}}{\rho}\Omega_s(cos\frac{\theta}{2} - cos\frac{\theta_{eq}}{2}) \tag{37}$$

When the system is under non-hydrostatic stress (i.e. grain contacts transmit stresses in excess of P_f van Noort et al. (2008)), the chemical drop that drives the neck growth can be written as

$$\frac{\gamma_{sl}}{\rho}\Delta_s(cos\frac{\theta}{2} - cos\frac{\theta_{eq}}{2}) - (\Delta f_s + P_f\Delta\Omega_s) \tag{38}$$

2.3.3 Grain boundary healing

E.g. Visser (1999); Koelemeijer et al. (2012); Houben et al. (2013) showed multiple ways for healing and sealing of cracks and permeability reduction. Note that we define healing as increase in strength, hence increase in elastic stiffness and sealing as decrease in permeability. Two ways for healing and sealing are:
(1) Elastic deformation, plastic flow or pressure solution due to an increase in mean normal stress resulting in a decrease in permeability can result in mechanical closure (e.g. Chen et al. (1996); Koelemeijer et al. (2012); Houben et al. (2013)).
(2) The reduction in surface energy could result in crack healing/sealing whereby the permeability was reduced and the strength restored (Houben et al. (2013)). Diffusive mass transport occurs through thin water films adsorbed to the solid surface, or through brine that fills the pores completely (island channel). When the grain contact zone exist of an island-channel, the system is in non-equilibrium (Visser (1999)). Lehner (1995) showed that the local stress induced forces need to be bigger than the internal free energy. When the grains are not under stress the islands will grow whereas the channels will shrink due to a resultant surface energy related force. Therefore the growth of the islands and occlusion of the channels will result under the influence of γ_{sl} will result in cementing up of the grain contacts as well. When the applied stress becomes below a critical value, the boundaries will close.
van Noort et al. (2008) supposed a criteria at which grain boundary healing occurred assuming an island channel structure at the contact between elastic solid grains. van Noort et al. (2008) assumed in this model that the individual island in the contacts were interpreted as small necks. Growth of these necks will result in grain boundary healing. The driving for for the grain boundary island growth that result in healing can be written as

$$\Delta\mu = \frac{2\gamma_{sl}}{\delta}\Omega_s(cos\frac{\theta}{2} - cos\frac{\theta_{eq}}{2}) - \frac{[(\sigma_n - P_f)/\alpha]^2}{2E}\Omega_s \tag{39}$$

Grain boundary healing will occur when the driving force is positive. A criteria for grain boundary healing is presented by van Noort et al. (2008) indicating the stress below which grain boundaries heal and van be written as

$$\sigma_{crit} = 2\alpha\sqrt{E\frac{\gamma_{sl}}{\delta}(cos\frac{\theta}{2} - cos\frac{\theta_{eq}}{2})} \tag{40}$$

Where α represents the total island area fraction, E Young's Modulus of salt, δ the grain boundary width, γ_{sl} interfacial energy between the solid and the liquid phase, θ the dihedral angle and θ_{eq} the equilibrium dihedral angle.

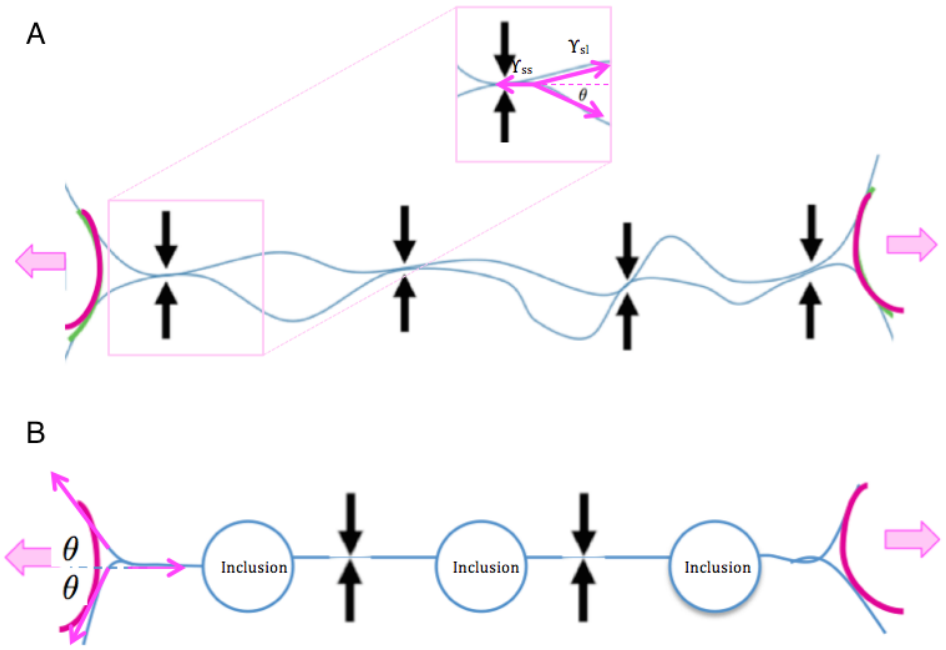

Figure 3: *Possible mechanisms operating when stress is applied on a solid-liquid NaCl system. A. Island channel grain boundary. A stress is applied on the contacts and pressure solution can occur. Healing will occur when a critical stress is reached and* $2\gamma_{sl}cos\theta > \gamma_{ss}$. *Neck growth can occur when* $\theta \neq \theta_{eq}$ *B. No pressure solution can occur, because material cannot be transferred to the pore wall areas. Healing can operate. Neck growth can occur when* $\theta \neq \theta_{eq}$.

3 Methods

3.1 Starting material

One dimensional compaction experiments were performed on four different grain size fractions of rock salt (Table 2) obtained by sieving the granular salt (AR grade NaCl; Merck Chemicals) in a low humidity room. The salt grains represent uncrushed cubic salt grains. However, at the smallest grain size fraction the cubic shape is not developed entirely whereby the grains seems partly crushed. No larger grain size fraction was used, because friction of the grains on the walls of the capillary tube would be too high in the case that there are not enough grains positioned next to each other. The granular salt was weighted on an analytical balance (accuracy 0.01g) and dried for one day in an oven of 50°C before use. For the long term compaction experiments, the granular salt was weighted on an analytical balance with an accuracy of 0.0001gram. The set up was weighted with and without the salt sample to calculate the exact weight of the sample. Initially saturated NaCl solution is used as a pore fluid and is obtained by adding AR grade NaCl to demineralized water till the solution becomes fully saturated. The grain size that is used to saturate the NaCl solution corresponds to the grain size fractions of the granular salt used in the compaction experiments. In this way we minimize the influence of the grains in the oversaturated brine solution on the compaction experiment.

3.2 Short term compaction experiments

The presented experiments consist of uniaxial (1-D) compaction experiments that were performed on granular salt under both wet and dry conditions whereby initially saturated NaCl solution and n-decane ($C_{10}H_{22}$) is used as pore fluid. The experiments were performed at room temperature under chemically closed-system conditions. The closed system indicates a simple drained system where the pore fluid is barely squeezed out during compaction (Meer and Spiers (1997)). This involves dissolution of material at grain contacts under high normal stress, diffusion through the grain boundary fluid phase and precipitation on the pore walls of grain contacts under low normal stresses (Meer and Spiers (1997); Spiers et al. (1990); Spiers et al. (2003)). The experiments were carried out on varying the applied stress (σ), the sample grain size (d) and the fluid type to get insight on the dependence of compaction creep behavior on these variables. Table 2 shows the different variables as used in the compaction experiments. The complete set of dry and wet experiments and the corresponding conditions and variables is shown in Table 4.

The compaction experiments were conducted at two different locations (i.e. Utrecht and Atlanta) and despite the temperature and humidity conditions varies slightly to location, the compaction results were reproduced without significant errors. All the uniaxial compaction experiments were performed at room temperature under dry and wet conditions, using a small scale, dead-weight, capillary tube set up (e.g. de Meer and Spiers, 1997; Visser et al., 2012) as shown in Figure 4. The capillary tube with a diameter of ∼1mm was used to apply stresses bigger than 0.811 MPa, while the tube with a diameter of ∼2mm was used to apply a stress of 0.175 MPa on the sample. Before setting up the material, the glass capillary tubes, pistons and brass base were rinsed carefully with demineralized water and n-hexane. The material was rinsed with n-hexane to remove all the (greasy) material to minimize the amount of friction on the salt grains. After rinsing the material, the material was dried for ∼ one day in the oven at 50°C.
In setting up the material, first the lower piston and the glass tube was placed in the brass base, followed by ∼0.02 gram (1mm tube) and ∼0.06 gram (2.1 mm tube) sample of the chosen grain size fraction that was funneled into the capillary tube to make sure that the start length of the sample was about 16mm. The upper piston and fluid reservoir were carefully placed on the top of the sample. An evacuation tube and syringe were attached to the brass base to flush the relevant fluid through the sample. This total setup was placed in a clamp stand. Before the initial stage of the experiment, the length of the sample was measured with a ruler. In the initial stage of each experiment, the sample was pre compacted dry for ∼30 minutes by a stress of ∼4.9 MPa to obtain a well controlled starting aggregate with reproducible porosity to eliminate inter granular rearrangements during later compaction (Zhang et al. (2002)). This led to a time independent compaction between 6 and 13% that resulted in a start porosity (ϕ_0) of ∼30%. The samples were unloaded and the initial length (L_i) of the samples was measured with a ruler. The porosity of the dry loaded samples was calculated from the initial length of the sample, the weight of the sample and the density of NaCl (2.17 g/cm^3). After the dry pre compaction, the samples were dry compacted for 10 minutes under a constant stress. The sample length was recorded every 60 seconds using the dial gauge meter and stopwatch during the dry compaction. The fluid (i.e. saturated NaCl solution or n-decane) was added, from above, in the fluid reservoir and introduced into the sample by sucking through the evacuation tube using the syringe. The sample length was recorded for 35 minutes under a constant stress every 30 seconds using the dial gauge meter and stopwatch during wet compaction. The wet compaction time for the n-decane saturated samples varies from 35 minutes to two weeks. The different stresses that are used correspond to 2.75, 1.88, 0.811 and 0.175 MPa. To confirm the dominant mechanism as shown by e.g. **?** at different volumetric strains, the compaction experiments were interrupted at volumetric strains of 0%, 3%, 6% and 9% for the grain size fraction 90 - 125 μm under an applied stress of 1.88 MPa. After conducting the experiments, the samples were flushed with n-hexane to remove all of the residual solution, dried in the oven of ∼ 50°C and impregnated with epoxy resin.

Table 2: *Variables as used during the short term uniaxial compaction experiments*

Parameter	Unit	Value			
Grain size	μm	50 - 90	90 - 125	125 - 150	50 - 150
Applied stress	MPa	0.175	0.811	1.88	2.75
Fluid type	-	Brine solution	Hydrocarbon		
Temperature	°C	Room temp.			

3.3 Long term compaction experiments

The long term uniaxial compaction experiments presented here were performed on granular salt under chemically closed system conditions. The complete set of wet experiments reported along with the corresponding conditions and variables is shown in Table 3.
Small changes were made for the long term compaction experiments. The long term experiments were performed at 40°C ($\pm 1°C$ in a temperature controlled box under wet conditions using the same set up as during the short term compaction experiments. The grain size is kept constant, while the applied stress varied. To prevent evaporation of the brine, silicon oil was place in the fluid reservoir after the sample was flushed with saturated brine. The set up was placed in the Uniaxial salt deformation apparatus to align the set up. During these experiments, gap sensors were used to log the displacement. To control the reproducibility, four long term compaction experiments were conducted. To minimize the effect of friction only 2mm tubes with graphite powder on the walls were used. Also, a small filter paper was placed between the sample and the upper piston to avoid grains between the upper piston and the glass tube and the sample length is reduced to 4 mm. The initial length and the length after pre compaction of the sample was measured by using a traveller microscope. The improvements in the experimental set up and procedure allowed us to calculated the porosity and measure the volumetric strain more accurately compared to the method of the short term experiments.

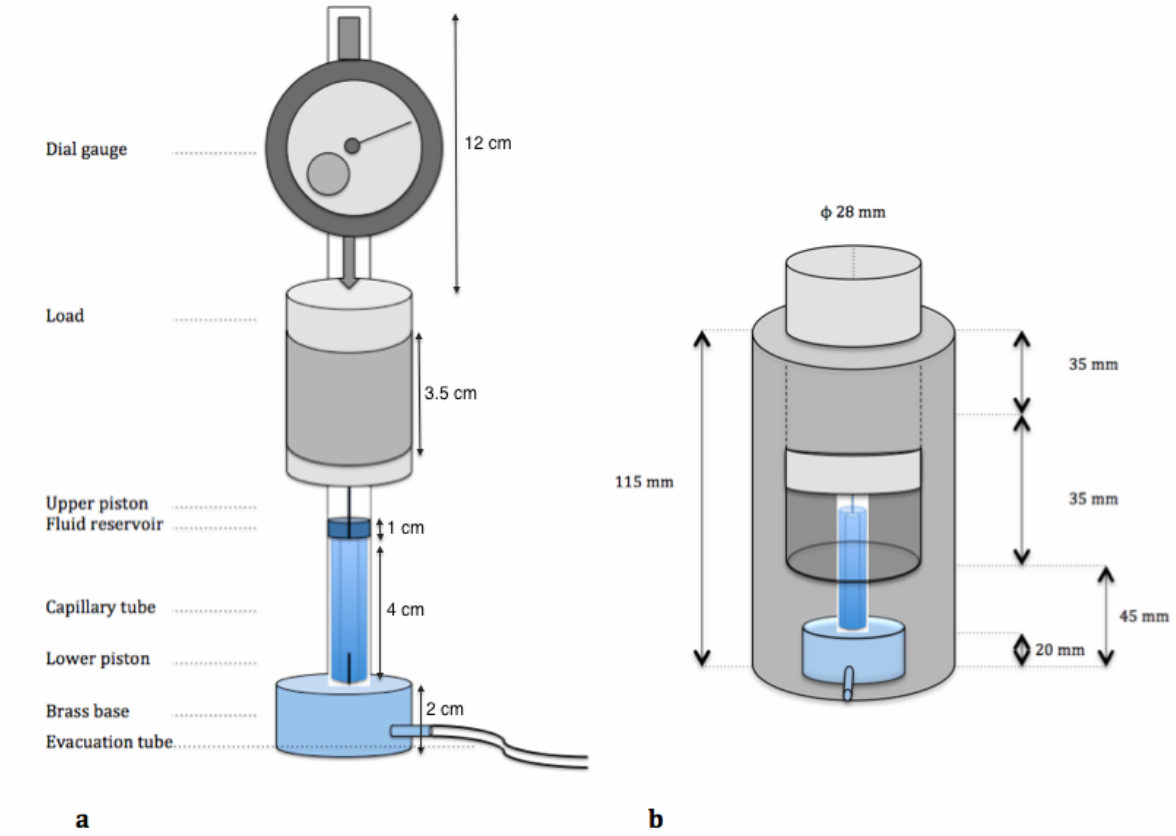

Figure 4: *Schematic illustration of the experimental set-up used for the uniaxial compaction experiments. (a) Complete experimental set-up; (b) Uniaxial Salt Deformation Apparatus (USDA)*

3.4 Microstructural methods

The starting material, dry-compacted and wet-compacted samples were studied by using the transmission optical microscopy (Leica DM750 & Koehler) at Georgia Tech and the Leica DC 300 at Utrecht University. The software LeicaQwin was used to image the samples. The thin sections that contain the saturated brine solution, oil filled compacted samples and pre compacted samples were prepared by flushing them with n-hexane to remove the residual brine solution and dried in the oven for ∼2days. After drying, the samples were impregnated with epoxy resin (Araldite A and B (100:30)), placed for ∼15 minutes in the vacuum chamber to saturate the entire sample with the epoxy resin and dried for ∼2 days at room temperature. Finally, the samples were cut with a diamond saw, sandpapered and polished by using SiC-800, 1200, 2500 and 4000 paper and diamond-polishing suspension (MetaDi Oil based 1μm). A volatile oil was used as lubricant and cooling agent while sandpapering the samples. While sandpapering the samples, the thin section holder and thin section it self were rinsed regularly with n-hexane to minimize the amount of scratches by loosen salt grains. The thin sections were stored in a low humidity room to prevent moister from getting into the sample. For the optical microscopy, a cover slip was glued onto the sample with glycerine, to prevent moisture from corrupting the microstructure into the sample during the observations. Attaching a cover slip increases the quality of the picture as well.

For grain size, pore space, grain contact area and orientation analysis, pictures were taken by the optical microscopy (Leica DC300) in transmitted light. In total 20 pictures were taken from one sample and stitched together (Microsoft Image Composite Editor) to get a high quality image of the entire thin section (Figure 18). The panorama picture was analyzed by using the computer program JMicroVision. About 500 grains were detected manually. Grains that were located at the sides of the sample (i.e. experience the highest friction) were excluded from analysis.

4 Mechanical results

4.1 Uniaxial compaction experiments performed using NaCl solution

The dry pre compaction stage produced an instantaneous reduction in the volume of the sample of ∼6 -13% to achieve a start porosity of ∼30% ±5% (Table 4). Samples with a start porosity outside the range were rejected. Also, all the experimental results with a grain size of 50 - 105 μm were rejected, because no representative compaction curve was obtained from these data. For all the samples no on-going compaction creep was observed during the dry creep stage. However, all the samples showed relatively rapid on-going creep from the moment that the saturated NaCl solution was flushed through the sample. The corresponding numerical data that was obtained by the experiments was used to construct plots of (1) Volumetric strain (e_v) versus time (t), (2) log strain rate($\dot{\varepsilon}$) versus log strain (ε), (3) log strain rate ($\dot{\varepsilon}$) versus log grain size (d) and (4) log strain rate ($\dot{\varepsilon}$) versus log stress (σ).
The instantaneous volumetric strain (e_v) was calculated directly from the displacement versus time data, measured during the uni-axial compaction experiments, and is equal to $e_v = -\Delta L/L$ (Visser et al. (2012)). Selections of representative compaction creep curves obtained from the flooded samples that illustrate the influence stress are shown in Figure 5. Reproducible experiments for each grain size and applied stress were conducted to make sure that the measurements were accurate. Under the same conditions, the experimental results deviate up to ∼ 0.2%. The compaction creep curves corresponding to a constant grain size distribution of 125-150 μm, 90 - 125 μm and 50 - 90 μm and applied stresses of 2.75, 1.88, 0.811 and 0.175 MPa are shown in Figure 5a, Figure 5b and Figure 5c respectively. The applied stresses causes effective volumetric strains (e_v) of ∼8.8%, 7.2%, 5.1% and 3% respectively for the grain size distribution of 125 - 150 μm, effective volumetric strains of ∼ 9.7%, 8.9%, 7.4% and 5% respectively for the grain size distribution of 90 - 125 μm and effective volumetric strains of ∼16%, 13.8%, 12.1% and 8.8% respectively for the grain size distribution of 50 - 90 μm. This means that an increase in compaction creep is promoted by (1) an increased applied stress (σ_a) and (2) a decrease in grain size (d).

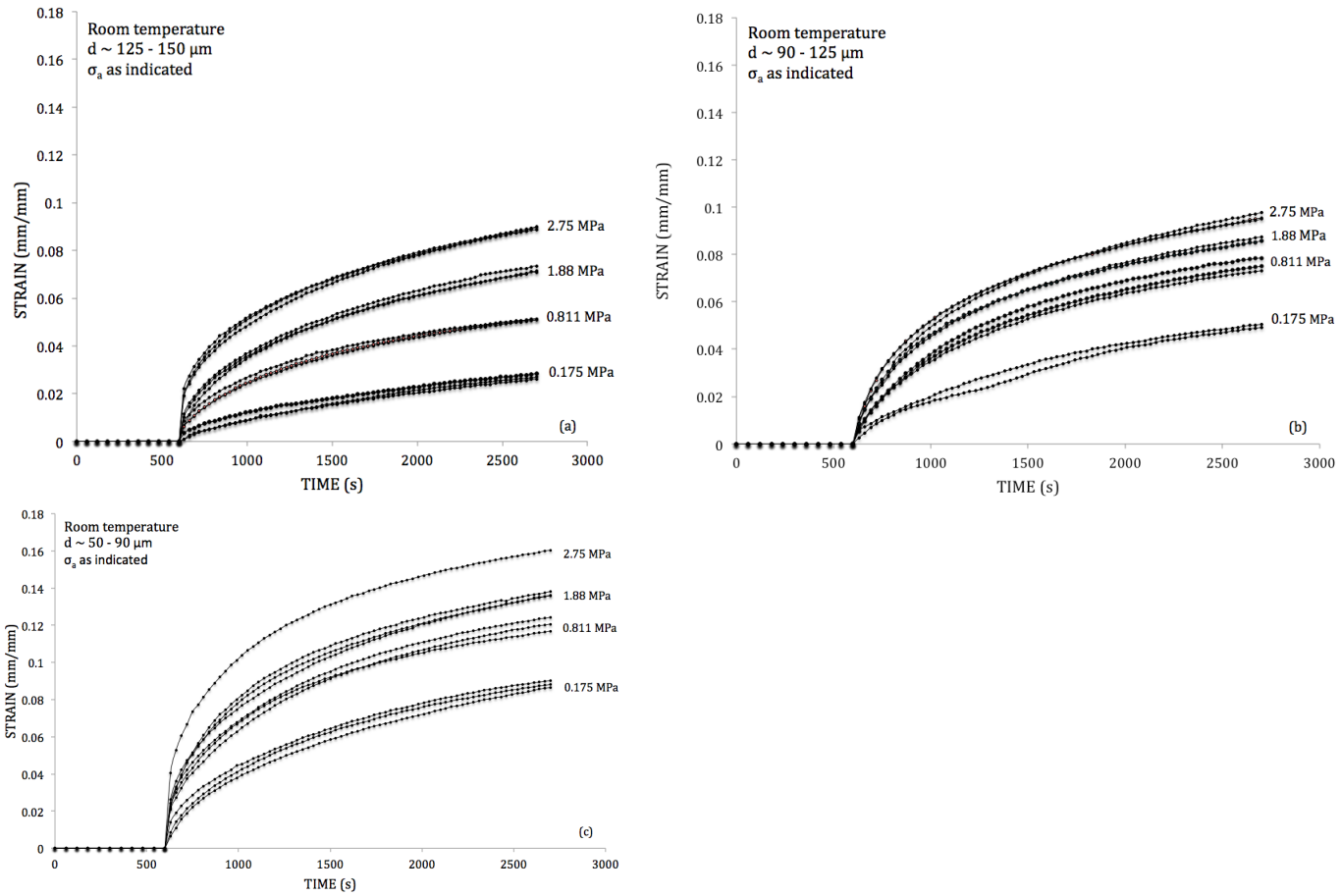

Figure 5: *Selection of representative compaction creep curves obtained by the uniaxial wet and dry compaction experiments on halite. Note the effects of increasing applied stress (σ_a) on the compaction creep. Grain sizes correspond to (a) 125 - 150 μm, (b) 90 - 125 μm and (c) 50 - 90 μm.*

The dependence of compaction creep rate on strain is derived from Figure 5 and illustrated in Figure 6 . By combining the strain rate ($\dot{\varepsilon}$) versus volumetric strain data it is possible to examine how the creep rate of wet samples depends on the applied stress (Visser et al. (2012)). Figure 6 illustrates how the compaction rate ($\dot{\varepsilon}$) at a fixed creep strain (e_v) increases with increasing applied stress (σ_a) and decrease in grain size. According to Visser et al. (2012) the correlation between the volumetric strain (ε) and the volumetric strain rate ($\dot{\varepsilon}$) can be described by a power law function of the form $\dot{\varepsilon} \propto e_v^k$, where k exponent represents the slope, $\dot{\varepsilon}$ the volumetric strain rate and e_v the volumetric strain. Figure 6 illustrates a varying slope for varying volumetric strains and grain sizes. The log-log plot for the grain size distribution of 125 - 150 μm, 90 - 125 μm and 50 - 90 μm is shown in Figure 6a and Figure 6b and Figure 6c respectively. The curves that represent the smallest grain size fractions (i.e. 90 - 125 μm and 50 - 90 μm) are all convex. The value of k is measured directly from the log-log plots and represents k = 1-2 is for volumetric strains of 2-6%, k=2-3 for volumetric strains of 5-10%, k=3-4 for volumetric strains of 8-11% and a k value of 4-5 for volumetric strains between 10-16% for the grain size distribution of 50 - 90 μm. The slope of the curves become steeper towards higher volumetric strains, which means that the strain rate decreases faster towards higher volumetric strains. Note that for the highest applied stress of 2.75 MPa the slope of the curve is the steepest at the moment that the fluid is flushed through the sample. The following slopes are found for the grain size distribution of 90 - 124 μm: k=2-2.5 for volumetric strains between 5 - 8%, k=1- 2 for volumetric strains between 2.5-5%. The slope of the log-log plots representing the grain size distribution of 125 - 150 μm is in general steeper and less concave for the same applied pressure compared to the log-log plots representing a smaller grain size (Fig. 6). For the grain size distribution of 125-150μm the following slope values are found: k = 0.5-1 is found for volumetric strains of 1-2%, k=1-2 for volumetric strains of 2-3% and k=2-3 for volumetric strains between 5 and 8%. For all of the applied stresses and the grain size distribution of 125 - 150 μm, the slope of the curves is the steepest at the moment the saturated NaCl solution is flushed through the sample. This means the the strain rate decreases the fastest after the reaction with the brine solution.

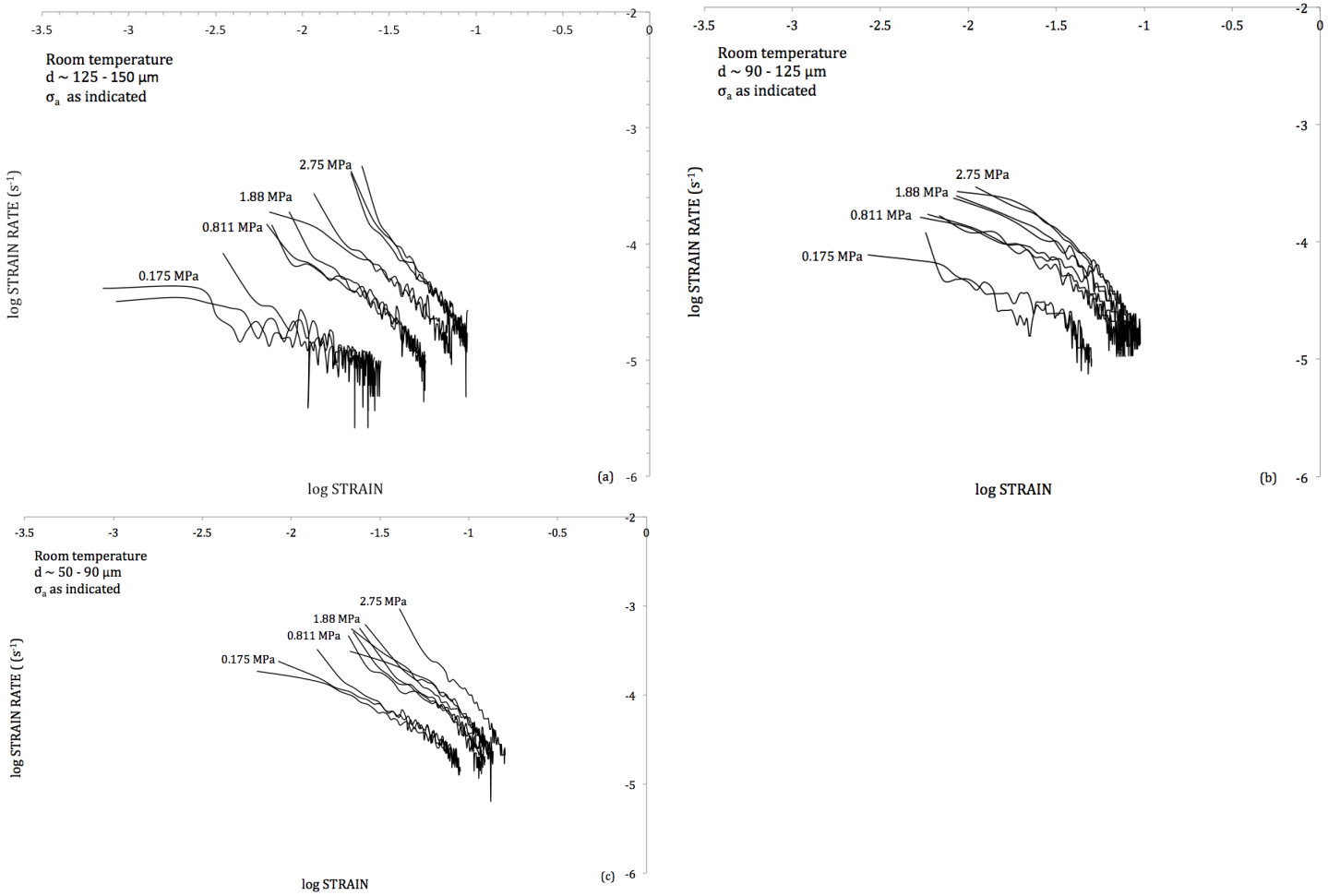

Figure 6: *Selection of representative log-log plots of compaction strain rate versus compaction strain constructed from the creep data presented in Figure 5. Grain sizes correspond to (a) 125 - 50 µm, (b) 90 - 125 µm and (c) 50 - 90 µm.*

In general, for all grain sizes and applied stresses we observed that the strain rate decreased faster towards higher volumetric strains resulting in a steepening of the slope. An increase in grain size will steepen the slope of the log-log plots as well. The steep slope of the log-log plots at the moment that the fluid is flushed through the sample indicates a fast compaction creep at the beginning of the experiment, followed by a rapid decrease in strain rate. This basically means that the sample reacts immediately on the presence of the saturated solution and enhances the pressure solution creep combined with a rearrangement of the grains. The strain rate decreases very quickly after the first measurement which result in a high k value at the beginning of the experiment. After a certain point, the curves are more convex. From that point on there is a faster decrease in strain rate towards higher volumetric strains.

The grain size dependence of volumetric strain rate is shown in log grain size log strain rate plots for a constant applied stress and volumetric strain and constructed from the compaction creep data of Figure 5 (Fig. 7). The average grain size for every grain size distribution (i.e. 70, 107 and 137 μm) is used to construct the curves. According to Visser et al. (2012), the correlation between the strain rate and grain size can be described by the power law function of the form $\dot{\varepsilon} \propto d^m$, where the m value represents the slope. For an applied stress of ∼1.88, 0.811 and 2.75 MPa an m-value of approximately -3 is observed and demonstrate that $\dot{\varepsilon}$ is approximately proportional to d^{-3} (Fig. 7a, b, c). For effective volumetric strains >6% and grain sizes >107 μm, an m value of about -1.5 is observed. For the grain size <107 μm an m value of about -3 is observed (Fig. 7a).

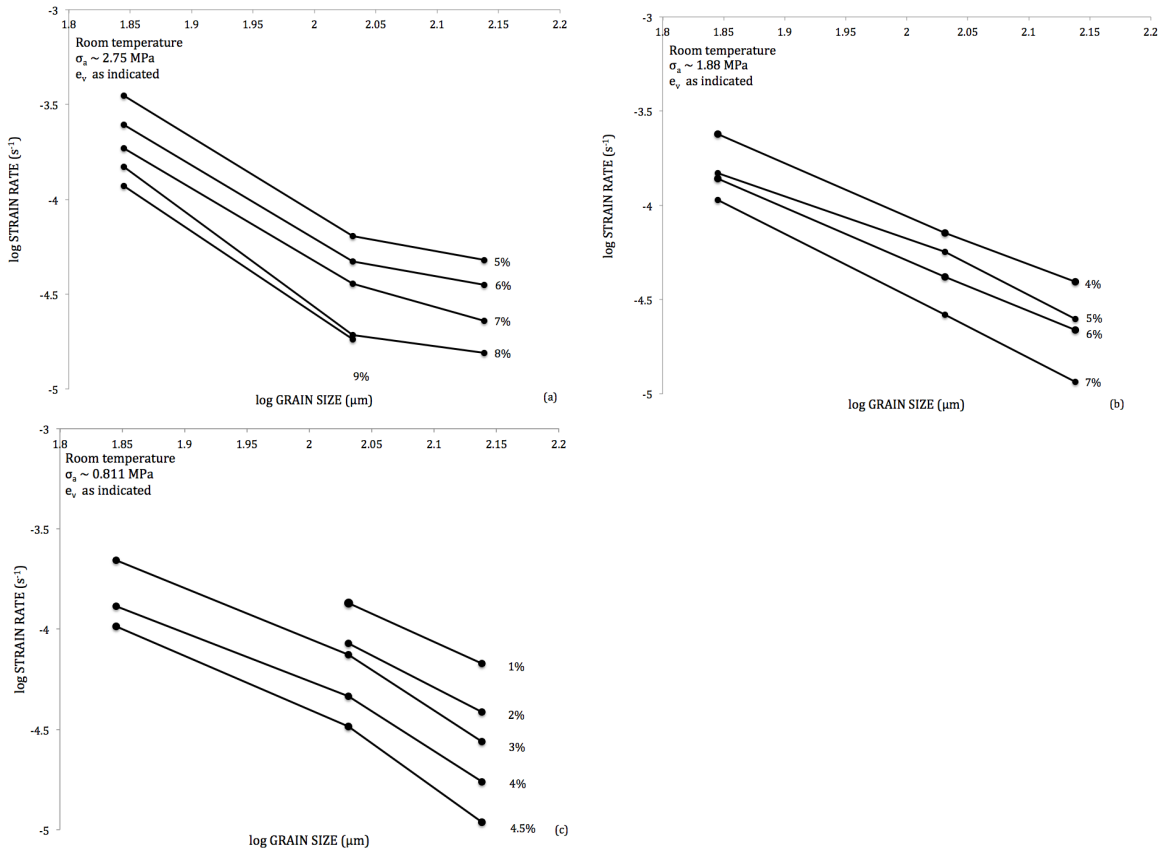

Figure 7: *Log-log plots illustrating the dependence of compaction strain rate on grain size. The applied stresses (σ_a) correspond to (a) 2.75 MPa and (b) 1.88MPa and (c) 0.811 MPa. The percentages next to the curves indicate the volumetric strains at which the data point was taken*

Log strain rate against log stress plots at fixed volumetric strain (3 - 12%), temperature (room temperature) and grain size (125 - 150μm; 50 - 90 μm) were derived from the data of Figure 6 and presented in Figure 8. The slopes of the curves plotted in Figure 8 represent the stress exponent (n) in an empirical power law description of the form $\dot{\varepsilon} \propto \sigma^n$ applied for a fixed volumetric strain and temperature (Visser et al. (2012)). The curves show an n value of 1 on average which indicates that the strain rate ($\dot{\varepsilon}$) is almost linear related to the applied stress (σ_a). For the larger grain sizes (125-150μm) the n value is somewhat more than 1 ($n \approx$ 1.1) and for the smaller grain sizes (50-90μm) the n value is somewhat less than 1 ($n \approx 0.9$).

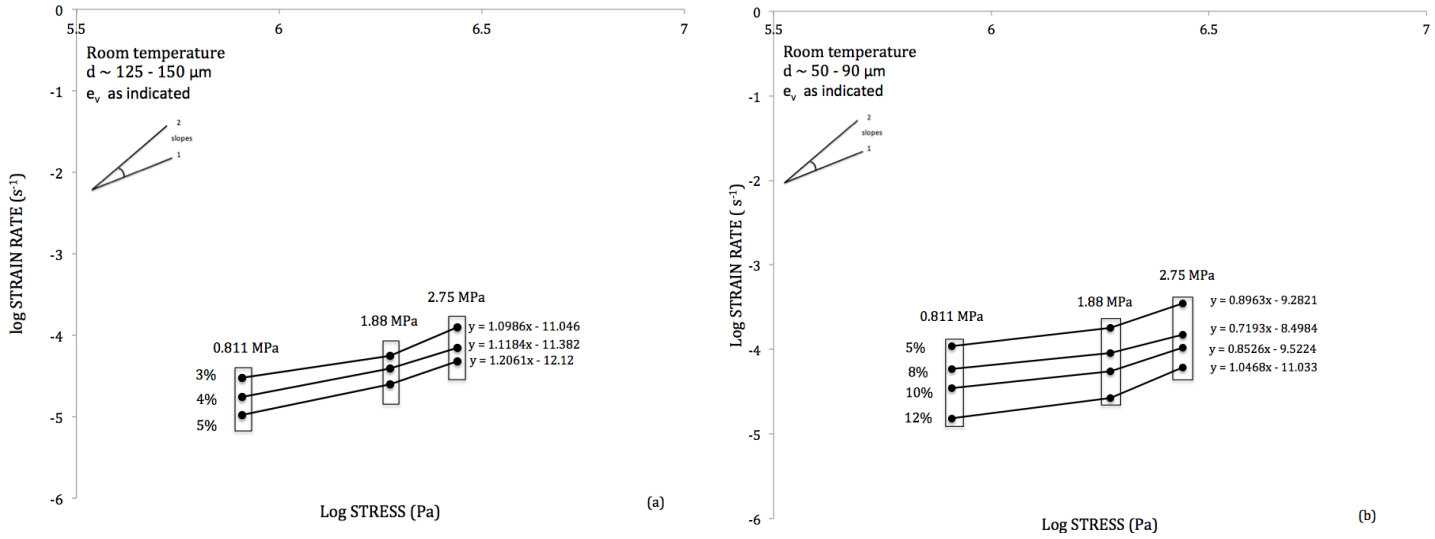

Figure 8: *Log-log plots of the strain rate versus applied stress for samples flooded with saturated brine solution. The volumetric strain and temperature are constant. The percentages indicate the fixed volumetric strain. Grain sizes correspond to (a) 125 - 150 µm and (b) 50 - 90 µm.*

4.2 Long term uniaxial compaction experiments performed using NaCl solution

For the long term compaction experiments we were able to calculate the start porosity more accurately. A start porosity of ∼42% ±5% was achieved. The start porosity for the short term compaction experiments was probably underestimated. The set of long term experiments with saturated brine solution along with the experimental conditions are given in Table 3. Even as the short term wet compaction experiments, rapid on-going compaction creep was observed until a certain volumetric strain was reached (Fig. 9). From this moment on the the volumetric strain decelerates until it stagnates. When plotting log strain rate versus log strain a change in slope (k) is observed. From a slope of ±1-2 for low volumetric strains to a slope of ±-7 for higher volumetric strains to almost a vertical slope (Fig. 9). The time porosity plot shows that for exp.022, the porosity becomes constant at at certain point. A higher stress was applied during exp.023, while the other parameters are kept constant. Figure 9 shows that a smaller porosity was achieved when a higher stress is applied on the system.

Table 3: *Variables as used during the long term uniaxial compaction experiments*

Sample name	Grain size (µm)	Start porosity (%)	Applied stress pre-compaction	Wet applied stress	Final porosity (%)
exp.021	63 - 71	44.60	3.85	1.08	18
exp.022	63 - 71	47.21	3.85	1.08	20
exp.023	63 - 71	40.54	3.85	3.03	4

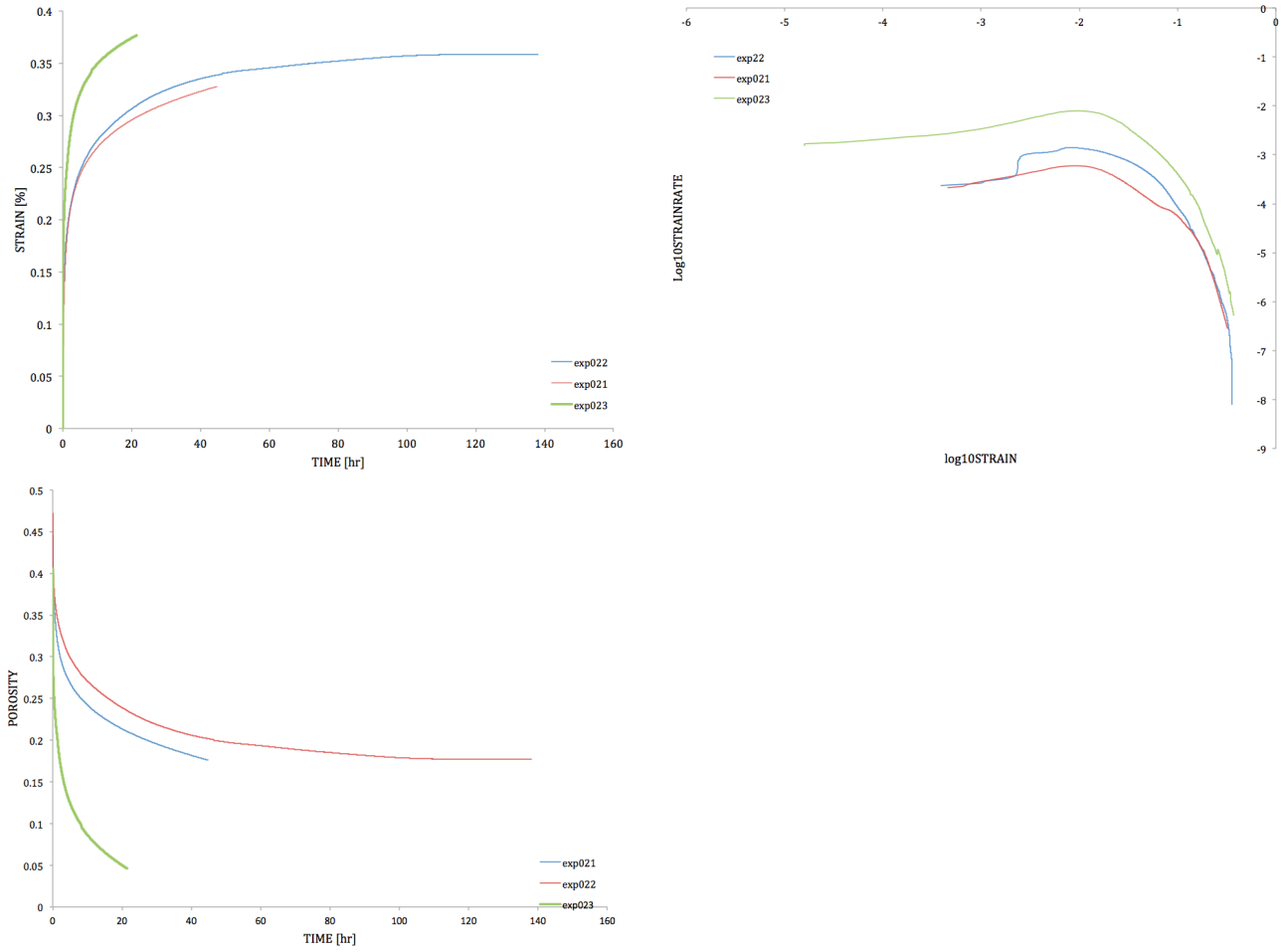

Figure 9: *Results of the long term compaction experiments. Top left: strain versus time; Top right: log_{10} strain versus log_{10} strain rate; Bottom left: porosity versus time.*

4.3 Uniaxial compaction experiments performed using n-decane

The complete set of experiments with added n-decane reported along with the corresponding experimental conditions and variables is shown in Table 4. During the dry pre compaction of $\sim$ 4.9 MPa, all the samples showed an instantaneous reduction in volume of $\sim$6 - 9% to achieve a start porosity of $\sim$25% $\pm$5% (Table 4). Minor creep was observed during the dry compaction stage. In contrast to the NaCl-saturated samples, the n-decane saturated samples showed no creep (Fig. 10. Because the uniaxial compaction experiments are carried out for only 35 minutes, no direct relationship with the compaction (rate) versus applied stress (σ_a) or grain size (d) was observed. For all the applied stresses and grain sizes a jump in the compaction creep curves is observed at the moment when the n-decane was flushed through the sample. This compaction probably indicates the rearrangement of the salt grains. $\leq$30seconds after the n-decane is added to the sample little or no creep is observed. Several samples in the addition of n-decane were compacted for a period of two weeks. Even after two weeks, no significant compaction was observed.

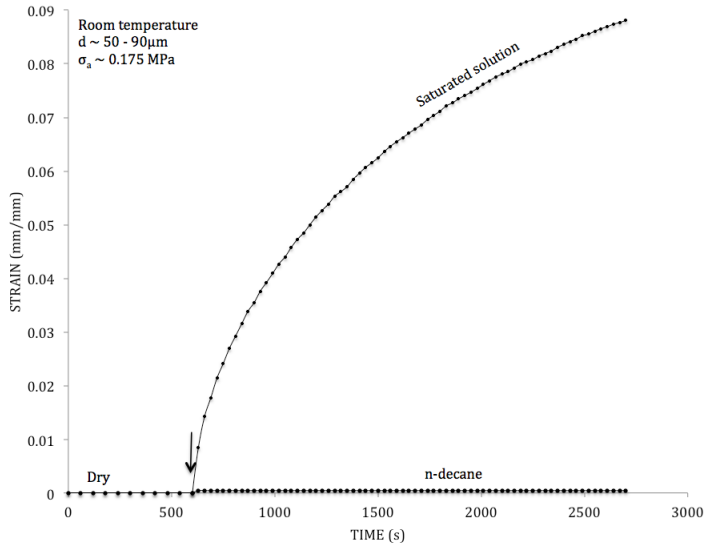

Figure 10: *Comparison of the compaction creep curves of granular salt loaded initially dry followed by saturation with n-decane versus granular salt loaded initially dry followed by saturation with brine solution. The creep curves are obtained by the uniaxial compaction experiments. The arrow indicates the moment when the fluid is flushed through the sample.*

5 Microstructural results

5.1 Optical microscopy

Microstructural analysis was performed on the sieved salt starting powder and compacted brine saturated material for the grain size distributions 50 - 90 μm, 90 - 125 μm and 125 - 150 μm and small volumetric strains ($e_v < 15\%$) by using optical microscopy (transmitted light). For the grain size distribution of 90 - 125 μm and a constant applied stress of 1.88 MPa was applied to investigate the microstructural evolution for volumetric strains ranging from 0% to 9%. The optical work on the compacted material was carried out using chemically polished and etched sections, as described in the microstructural methods.

5.1.1 Starting powders

The sieved starting powder was spread on a glass plate and observed by using the optical microscope (transmitted light) to observe the grain shape and size of start material. The starting powders represent sieved fractions that consist of granular aggregates. The starting powder with grain size distribution of 90 - 125 μm shows semi equi-axed particles with reasonable uniform size (Fig. 11a). The grain shape varies but shows mainly near cubic and rectangular shapes. Some angular shapes and broken grains were observed. The edges of the majority of the cubic and rectangular grain shapes are near rounded. The starting powder with the grain size distribution of 50 - 90 μm shows more irregular, angular and broken salt grains compared to the larger grain size fractions. Only a few near cubic grains are observed (Fig. 11b). The particles of the 50 - 90 μm grain size distribution shows non equi-axed particles and a poor uniform size. For all the grain size fractions, occasional pressure solution like microstructures are observed in the starting powders.

5.1.2 Dry compacted samples

Thin section studies were carried out on a dry compacted sample with grain size distribution of 90 - 125 μm to asses additional deformation mechanisms besides inter granular sliding rearrangement and to observe the shape of the grains. The dry sample is pre compacted for 30 minutes under an applied stress of $\sim$ 5 MPa en represents a volumetric strain of 0% and a start porosity of $\sim$ 30%. A tube with the diameter of $\sim$ 2 mm is chosen to make it easier to get the sample out of the tube since the sample is only pre compacted. Figure 12 shows the granular/porous microstructure of the pre compacted sample. The lighter parts in the picture represents the grains and the darker part the epoxy filled pores. The black dots are probably air bubbles that arise in the epoxy. The grains are randomly packed and have no preferred orientation. The pores between the grains are relatively big, since the sample is only pre compacted. As in the sieved starting powder, the shape of the grains varies from near cubic to irregular broken fragments with surrounded and angular edges. Only occasional pressure solution like microstructures as truncations and indentations are observed in the dry compacted sample.

Table 4: *Selected set of experiments with saturated NaCl solution and n-decane reported along with the corresponding experimental conditions and variables.*

Sample Number	Grain size (μm)	Applied Stress Pre-compaction (MPa)	Start porosity (%)	Wet and Dry Applied Stress (MPa)	Final (wet) Volumetric Strain (%)	Time Independent Compaction (%)
011214-4	125-150	4.99	29	2.75	8.99	6.25
011214-5	125-150	4.99	29	2.75	8.97	6.25
011214-7	125-150	4.99	29	2.75	8.86	6.67
021214-9	125-150	4.99	31	1.88	7.35	6.06
021214-11	125-150	4.99	26	1.88	7.13	6.06
021214-12	125-150	4.99	31	1.88	7.07	6.06
041214-17	125-150	4.99	29	0.81	5.08	6.25
041214-18	125-150	4.99	26	0.81	5.14	5.90
041214-20	125-150	4.99	29	0.81	5.14	5.90
051214-22	125-150	4.69	34	0.18	2.84	6.67
051214-23	125-150	4.69	37	0.18	2.62	7.15
091214-26	125-150	4.69	34	0.18	2.69	6.67
101214-30	50-90	4.69	32	0.18	9.02	13.3
101214-31	50-90	4.69	33	0.18	8.81	13.3
101214-32	50-90	4.69	34	0.18	8.66	13.3
111214-33	50-90	4.99	33	0.81	12.06	11.2
111214-34	50-90	4.99	29	0.81	12.43	11.8
111214-35	50-90	4.99	33	0.81	11.69	11.8
151214-37	50-90	4.99	26	1.88	13.62	13.3
151214-38	50-90	4.99	33	1.88	13.60	11.12
151214-40	50-90	4.99	29	1.88	14.47	11.8
161214-41	50-90	4.99	29	1.88	13.81	11.8
171214-44	50-90	4.99	26	2.75	16.04	12.5
060115-45	90-125	4.99	33	2.75	9.97	6.0
060115-46	90-125	4.99	24	2.75	9.76	7.15
060115-48	90-125	4.99	26	2.75	9.53	6.25
070115-49	90-125	4.99	26	2.75	9.50	6.7
070115-51	90-125	4.99	26	1.88	8.74	5.6
080115-54	90-125	4.99	26	1.88	8.57	6.7
080115-55	90-125	4.99	33	1.88	9.22	6.0
060115-57	90-125	4.99	30	1.88	8.97	6.0
090115-60	90-125	4.99	30	0.81	7.86	6.0
120115-62	90-125	4.99	26	0.81	7.50	6.3
120115-64	90-125	4.99	30	0.81	7.31	6.0
120115-65	90-125	4.99	30	2.75	4.92	7.15
130115-66	90-125	4.99	30	2.75	5.06	6.0
1decane	125-150	4.99	33	2.75	0.24	6.0
3decane	125-150	4.99	26	0.45	0.18	6.0
4decane	125-150	4.99	25	0.45	0.33	6.0
5decane	125-150	4.69	30	0.18	0.00	9.0
6decane	50-90	4.69	33	0.18	0.41	7.7
7decane	50-90	4.69	27	0.687	0.042	7.7

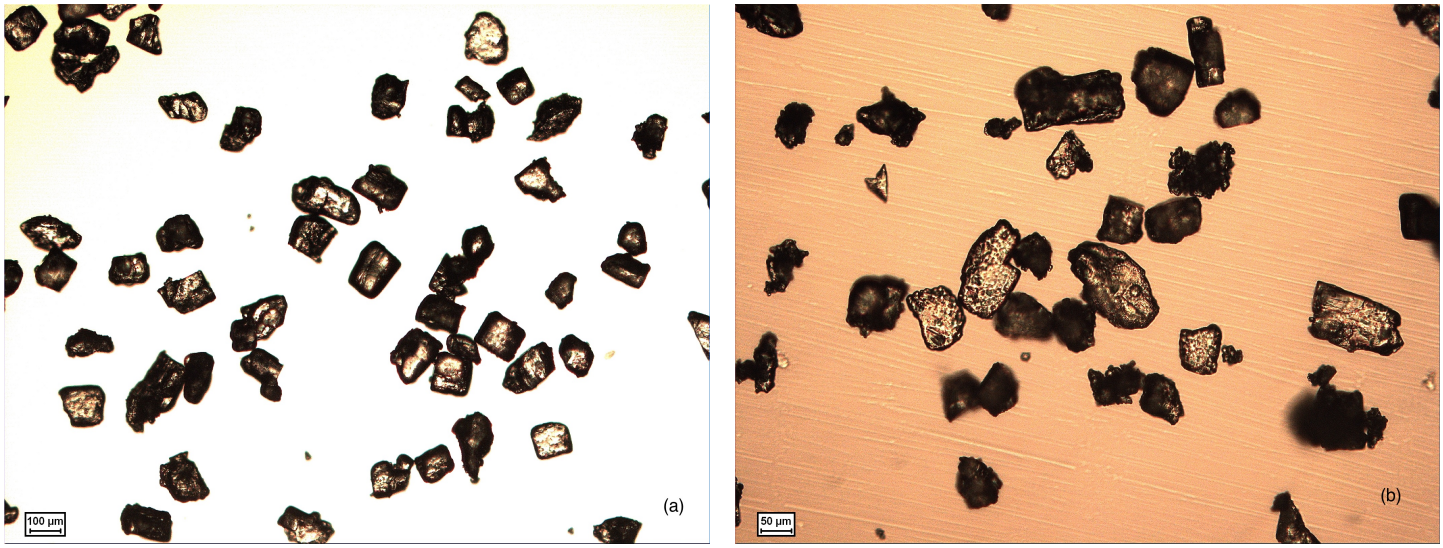

Figure 11: *Optical microscope images of dry and wet compacted samples. (a) Sieved NaCl powder whereas d = 90 - 125 µm (b) Sieved NaCl powder. Grainsize distribution is 50 - 90 µm*

5.1.3 Wet compacted samples

Microstructural analysis was performed away from the walls, because the grains on the edges (i.e. closesd to the tube wall during compaction), show an alignment of grains and a higher degree of pressure solution. These grains encounter friction of the tube during compaction and are not representative to describe the deformation mechanism. Different microsctructural regimes were observed in the wet compacted samples, depending on volumetric strain, grain size, applied stress and time.

Low volumetric strains (e_v <10%)

Samples with a constant grain size fraction (d = 90 - 125 μm) and constant applied stress (σ_a = 1.88 MPa) were observed at different volumetric strains to asses additional deformation mechanisms. The compaction experiments were stopped at different time intervals, and so different volumetric strains before were reached. The microstructural evolution from volumetric strains of 0% to 9% under the same conditions is shown in Figure 13b - c. The grain shape for the e_v = 3% sample is more or less similar to the dry compacted sample. All the wet-compacted samples examined show typical pressure solution features, such as contact truncations, grain-to-grain indentations (Fig. 13 b - c). The amount of pressure solution features increases in combination with a denser structure (e.g. Visser et al. (2012), Spiers et al. (1990)). Figure 13c shows the microstructure of a volumetric strains of 6% with relatively more pressure solution like structures in the sample.

Intermediate volumetric strain (e_v15%)

Microstructural analysis was done on the NaCl samples with a grain size distribution of 50 - 90 μm that are pre-compacted for 30 minutes under an applied stress of $\sim$ 5 minutes and wet-compacted under different applied stresses (σ_a = 0.175 MPa; σ_a = 1.88 MPa) for a time period of 35 minutes. The start porosity of the sample was $\sim$30%. For this finer grain size distribution, higher volumetric strains ($e_v \sim$ 15%) were reached in the same time compared to the medium grained samples (d = 90-125 μm). Fig. 14d shows clear evidence for grain growth by faceted overgrowth structures in the pores (indicated by 'o'). The small bridges that were clearly visible in Fig. 14d refer to neck growth (indicated by 'n'). Both necking and overgrowth features can result an increase in grain size. Almost all the grains are connect because of crystal growth. Even as the medium grained samples, the finer grained samples show typical pressure solution features such as grain-to-grain indentations, truncations and dissolved grain boundaries.

High volumetric strains (e_v=32%)

Figure 15 shows the microstructure of exp.21 whereby 32% strain was reached. A dense structure of well fitted grains was observed. The grains in this dense interlocking structure show a mixture of concave and convex grain boundaries and some triple junctions (Fig. 15;18). A large spread in grain size was observed. Subgrains en some neck features were observed as well (Fig. 18) The morphology of the grains has changed compared to the morphology of the grains at lower volumetric strains, namely from rectangular grains to more irregular grains at higher strains.

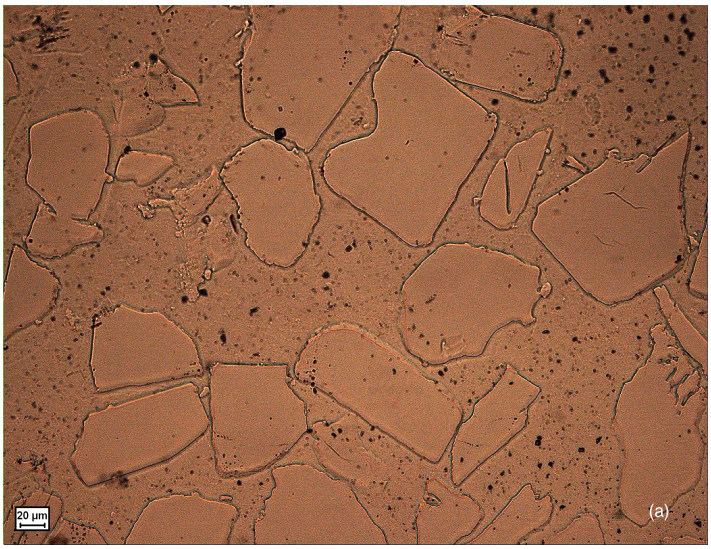

Figure 12: *Optical microscope images of the dry NaCl pre-compacted under an applied stress of 4.9 MPa and with a grain size range of 90 - 125 µm. From the orientation of the images, the stress is applied from the left/right for all the images.*

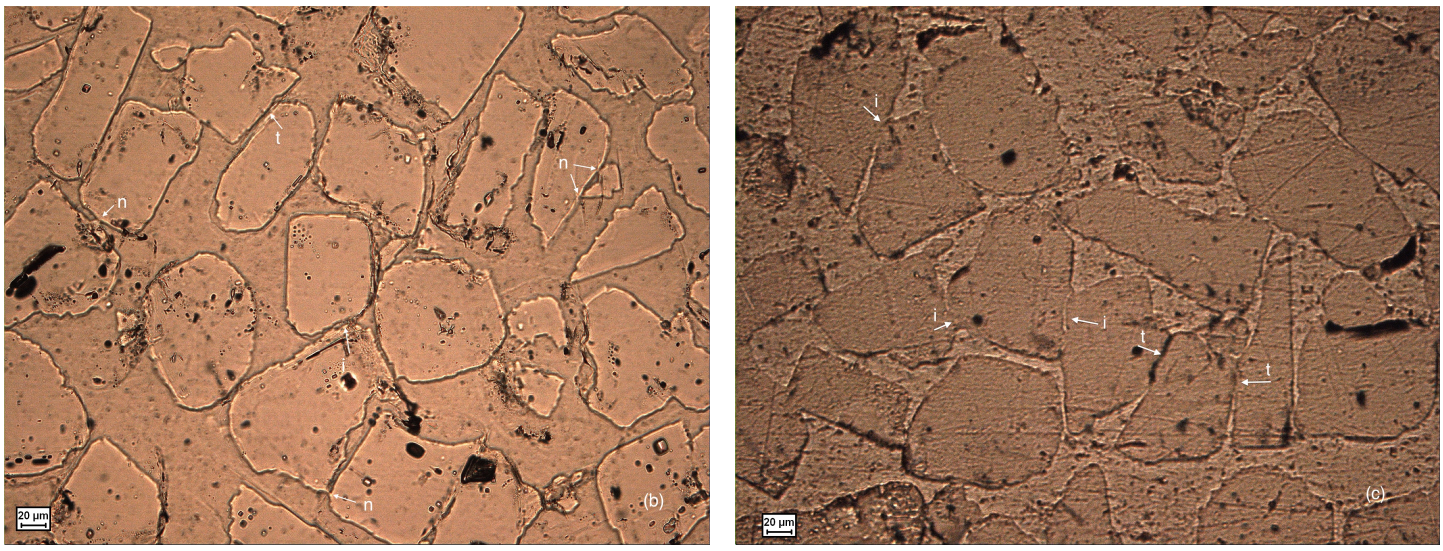

Figure 13: *(b) Wet- compacted NaCl grains under an applied stress of 1.88 MPa for ∼ 5 minutes up to 3% volumetric strain displaying porous aggregates with pressure solution like structures (indentations (i) and truncations (t)).(c) Wet-compacted NaCl grains. Wet-compacted under an applied stress of 1.88 MPa for ∼ 16 minutes up to 6% volumetric strain displaying a major amount of pressure solution like structures and a denser structure than in (b).*

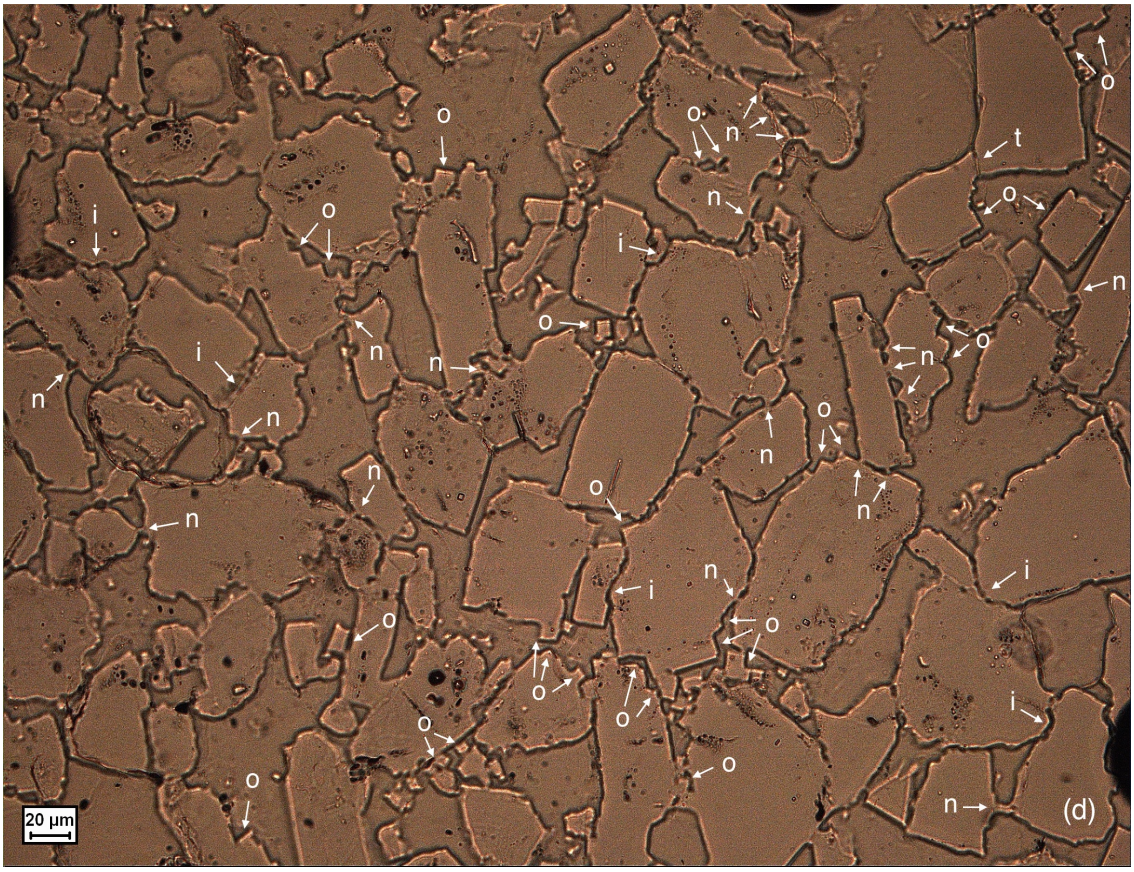

Figure 14: *Optical microscope image of were compacted NaCl under an applied stress of 1.88MPa with a grain size range of 50-90µm. Typical pressure solution features such as grain-to-grain indentations (i), truncations (t) and dissolved grain boundaries were observed. Also, neck growth (n) and overgrowth structures (o) were visible.*

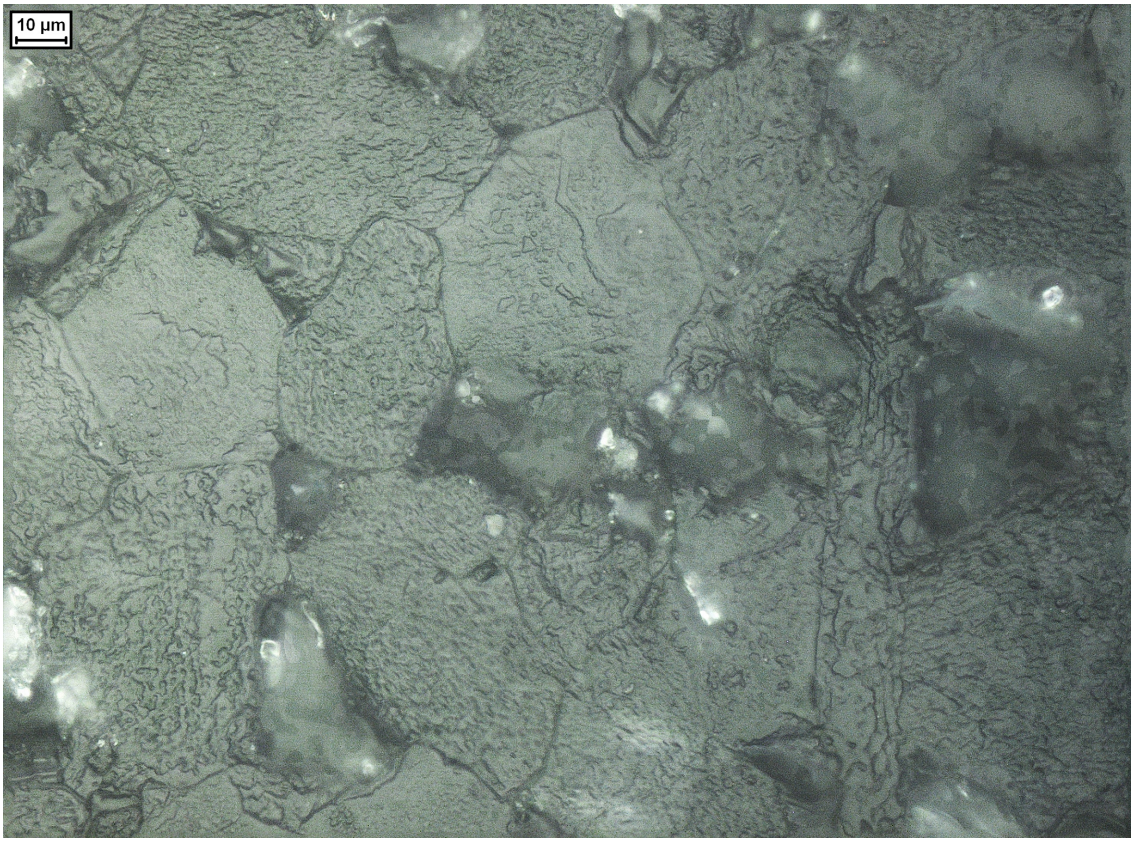

Figure 15: *Etched microstructure of exp.21, representing high volumetric strains (32%). A dense structure with well fitted grains, triple junctions and grain boundary migration was observed.*

5.2 Image analysis

The thin sections representing volumetric strains of 0%, 6% and 9% were wet compacted under the same conditions and used for further analysis by the computer program *Jmicrovision*. Also, the thick section representing higher volumetric strains (32%; exp21) was analyzed. Multiple pictures were taken from one thin section and stitched together to create a panorama (Fig. 18). The images were cropped for analysis so that the grains on the side of the sample (i.e. the grains that underwent friction from the side of the glass tube) were excluded from analysis. The perimeter of the grains and the contact lines were detected manually. About 500 grains need to be analyzed per thin section to be representative. For *Sample 2* and *Sample 3* less than 500 grains could be detected, because no more grains where present. Figure 18 shows that the grains present on the sides of sample 1 and sample two were colored black. SEM analysis didn't show evidence that chemicals (e.g. Fe-ions derived from the pistons) influenced the thin sections. According to the SEM image taken from *Sample 1* (Fig. 16) it is more likely that the grains on the side of the sample are dissolved. Therefore, the black grains that were present represent gaps originated from salt grains in the thin section. In sample 3, all salt grains that were present at the surface are dissolved (Fig. 18bottom). Table 5 shows the compaction conditions and values of parameters analyzed by Jmicrovision. Grain analysis shows a decrease in porosity with increasing volumetric strain. The average grain size was defined by the diameter of a circle with the same areas as that of the object and has a value of about 90μm, equal to the minimum fraction of the sieved grain size distribution.

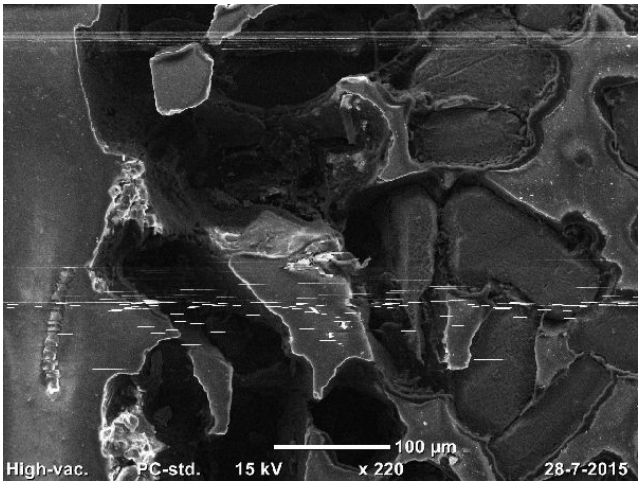

Figure 16: *Image taken by the SEM. The black holes represent dissolved salt grains.*

Table 5: *Compaction conditions and values of parameters as analyzed by Jmicovision*

	Unit	Sample 1	Sample 2	Sample 3	exp.21
Grain size	μm	90 - 125	90 - 125	90 - 125	63 - 71
Applied stress	MPa	1.18	1.18	6.5	1.08
Volumetric strain	%	0	6	9	32
Porosity	%	45.47	37.4	30.94	19.97
Contact line length (sum)	μm	11060.71	16847.76	11106.08	
Equivalent circular diameter (avg.)	μm	89.45	84.86	90.95	48.0
Amount of analyzed grains	-	687	458	368	287

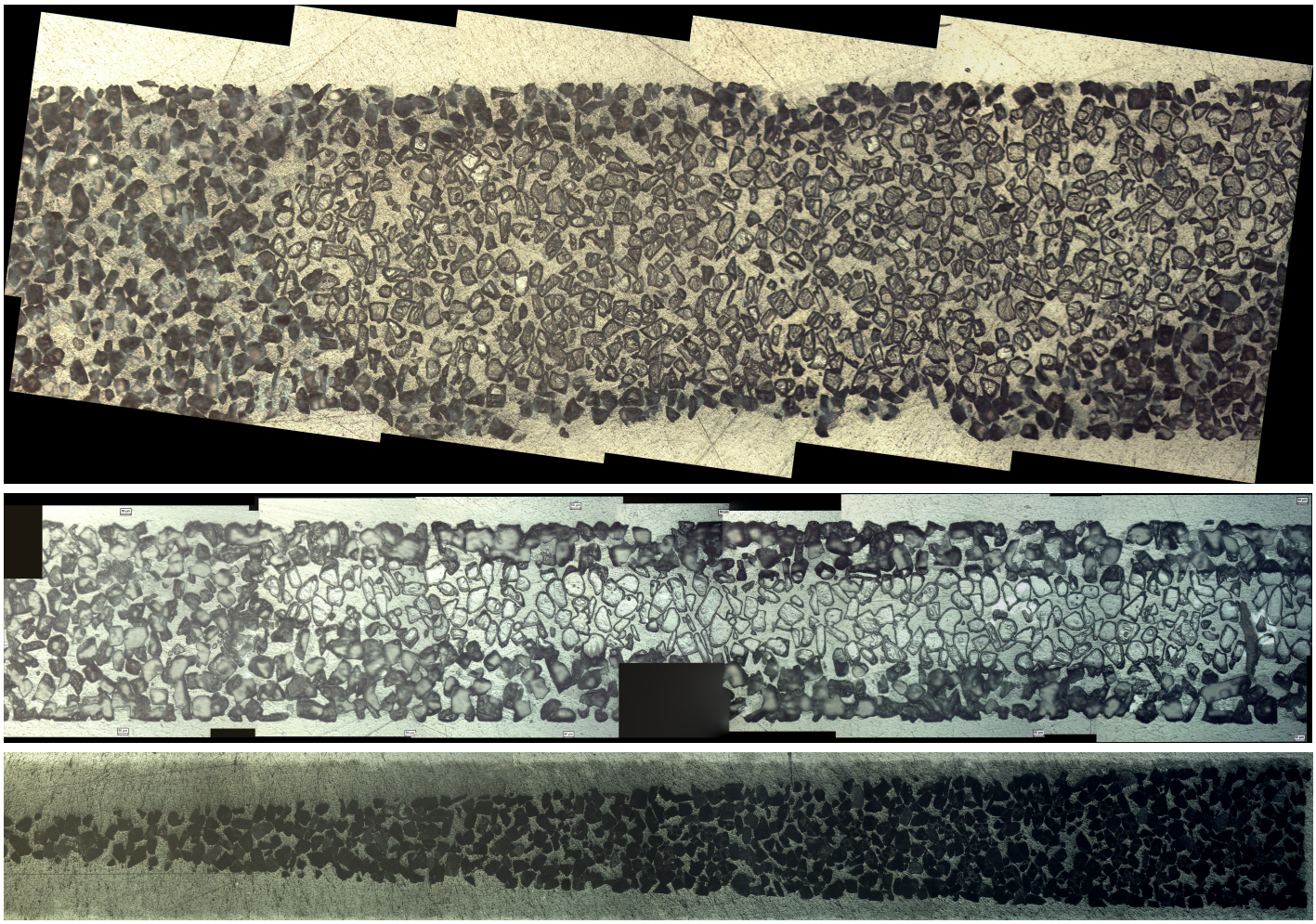

Figure 17: *Panorama of thin sections. From top to bottom: Sample 1 - Grain distribution after pre compaction (i.e. e_v=0%); Sample 2 - Grain distribution at e_v = 6%; Sample 3 - Grain distribution at e_v = 9%*

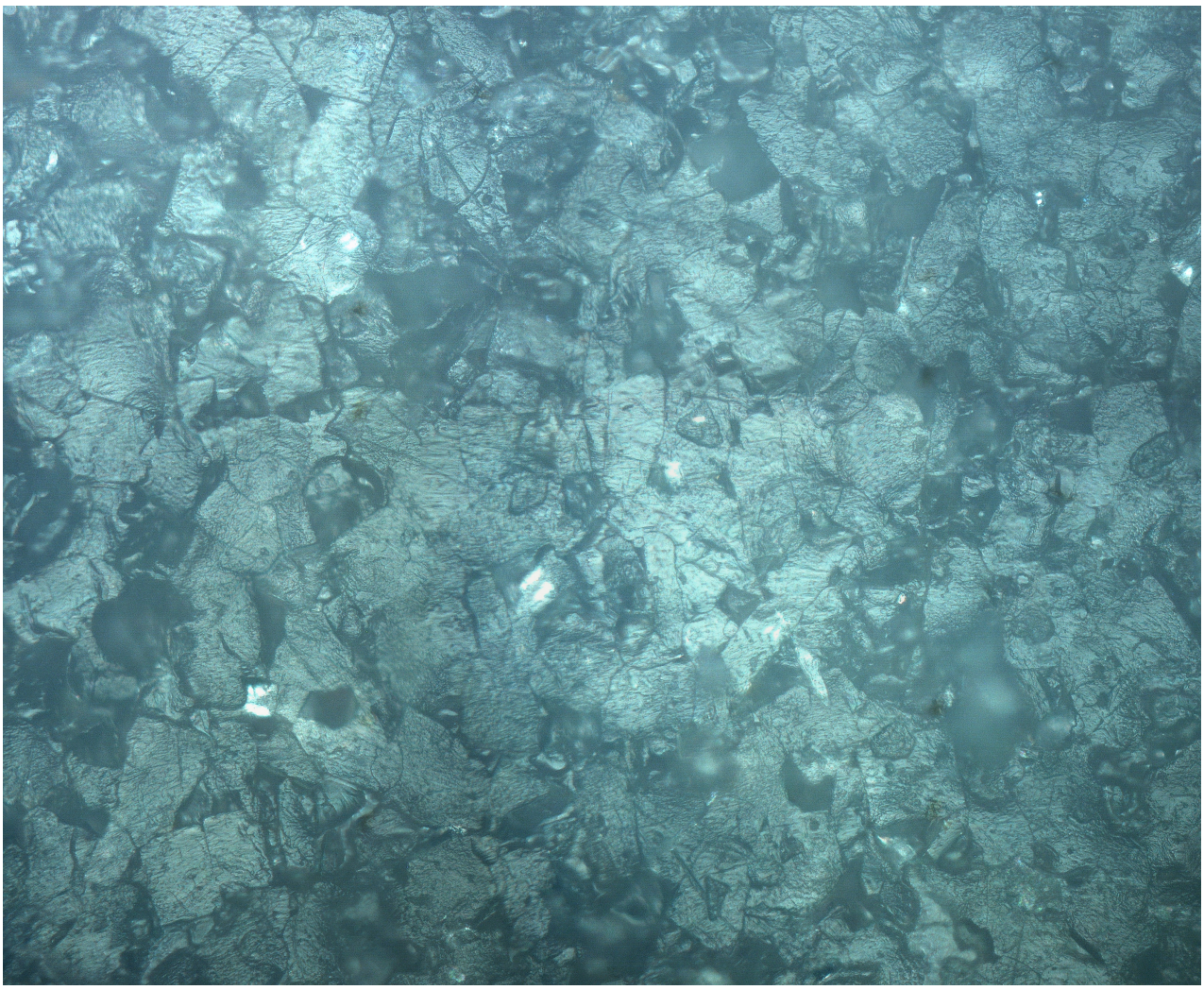

Figure 18: *Panorama of etched thick section representing exp.21. The grain size distribution was 63-71 μm and e_v=32%. Compaction was from the left.*

6 Discussion

The results obtained by the uniaxial compaction experiments demonstrated that dry, granular salt aggregates with a start porosity of about 30%, do not show compaction creep when loaded dry at stresses up to 4.9 MPa. Even as the dry compacted granular salt aggregates, the addition of n-decane shows no compaction creep at stresses up to 4.9 MPa for different grain size fractions and different time periods. The minor densification creep suggest that any purely mechanical effect of adding n-decane can be eliminated. The granular salt will deform mechanically as it deforms under dry conditions due to compaction of the bulk rock by elastic deformation or crystal plasticity, diffusive mass transfer and recrystallization (Houben et al. (2013)). Houben et al. (2013) shows that processes as diffusive mass transfer and recrystallization are relatively slow under dry conditions. This is consistent with the results obtained with the uniaxial compaction experiments under dry or oil saturated conditions, whereby almost no ongoing creep is observed. The microstructural observations show evidence that no fluid enhanced deformation is going on, because of the lack on pressure solution like structures. In contrast to dry and n-decane saturated samples, the addition of saturated NaCl solution enhanced the compaction creep. The rapid compaction rate suggests a fluid enhanced deformation process and is probably related to inter crystalline effects such as enhanced grain boundary diffusion or solution precipitation effects (Ter Heege et al. (2005); Visser et al. (2012)). The presence of indentations, truncations, overgrowths and necking structures that are observed during microstructural observations indicate that grain boundary diffusional pressure solution plays an important role during the densification (Visser et al. (2012)). However, the long term experiments show that the experiments stopped creeping when a porosity of ∼20 was reached. Experiments conducted with higher stress stopped at lower porosities (∼5%).

The discussion consist of different subsections to investigate the different mechanisms acting for at different strains (i.e. porosities). First of all, the experimental compaction data was compared with the pressure solution theory that ables us to test the applicability with the models of Spiers et al. (1990) and Pluymakers and Spiers (2014). The phenomological coefficient was determined by fitting the experimental data to both diffusion controlled compaction creep models. Second, the results of the microstructures were evaluated. Based on the microstructural observations, the contact area and grain contact area and surface energy are defined and tested for both analytical models. An estimation of the densification time was made based on the model of Spiers et al. (1990) and Pluymakers and Spiers (2014). Finally, the mechanisms operating till full densification were defined by conducting long term compaction experiments and tested for the healing criteria as published by van Noort and Spiers (2009).

6.1 Experimental results versus pressure solution theory

6.1.1 Theoretical model - Spiers et al. (1990)

The addition of the saturated brine solution enhanced the compaction creep and results in ongoing creep that is promoted by an increase in applied stress and a decrease in grain size (Fig. 5). The enhanced compaction creep suggests that a fluid enhanced deformation process as pressure solution is the rate controlling deformation mechanism in the uniaxial compaction experiments (Visser et al. (2012)). To verify that a fluid enhanced deformation process is the rate controlling mechanism and which deformation mechanism controls the rate, the experimental data is compared to the theoretical model of Spiers et al. (1990).

The slope of the presented curves in Figure 8 can be related to the mechanism that controls the compaction creep. The data presented in Figure 8 shows an average n-value of 1 for a fixed volumetric strain, temperature and grain size. According to the theoretical model presented by Spiers et al. (1990), a slope value of $n = 1$ represent diffusion, dissolution and precipitation controlled pressure solution. The deformation mechanism that controls the rate is either interface controlled pressure solution or diffusion controlled pressure solution for the presented compaction experiments with added NaCl solution. The reported data shows that for values of e_v between 3 and 15%. The compaction creep behavior of our wet samples can be described by an empirical constitutive equation of the form (Spiers et al. (1990))

$$\dot{\varepsilon} = B\frac{-M/T}{T}\frac{\sigma_c^n}{d^m e_v^k} \tag{41}$$

Where according to the reported data k ∼2 for e_v of 3-10% and k ∼4 for e_v=11-15% (Fig. 6), m ∼3 (Fig. 7), n ∼1 (Fig. 8). B and M are defined as the geometric constants. The results obtained by the compaction experiments in this report, agree to the theoretical model for diffusion controlled pressure solution as shown in equation (16) and to the results found by Spiers et al. (1990).

The phenomenological coefficient (Z^*) determines the absolute rate of creep and is a thermally activated term that represents the effective diffusivity along grain boundaries ($Z^* = Z_0 exp(-\Delta H/RT)$ (Spiers et al. (1990)) and can be estimated for the reported data by the function of compaction creep for porous aggregates given by

$$\dot{\varepsilon} = AV_m\frac{Z^*}{T}\frac{\sigma_a}{d^3 e_v^2} \tag{42}$$

The value of the parameters used are displayed in Table 6. Spiers et al. (1990) obtained a phenomenological coefficient with a value between 1.78×10^{-19} and 5.91×10^{-20} $m^3 s^{-1}$. In this report, the phenomenological coefficient is estimated by fitting the model of Spiers et al. (1990) (equation (28)) to test the applicability of the model. The experimentally measured porosities ($\phi_0 and \phi$) are used to cast the experimental data in the form of log strain rate versus log porosity for the different grain size ranges (Fig. 19). Figure 19 shows the log strain rate vs log porosity graph for the grain size distribution of 50 - 90 μm obtained by the experimental data. A Z^*-value for the grain size distribution of 50 - 90 μm of $1 \times 10^{-19} m^3 s^{-1}$ is calibrated. Note that the best fit for this grain size distribution and applied stresses is obtained for porosities $\sim$ <28%. For the grain size distribution of 90 - 125 μm a Z^*-value of 3×10^{-20} is calibrated. Note that the calibration for this grain size distribution consist of a narrow range of porosity differences. The Z^* obtained for this grain size is therefore not that accurate as for the smaller grain size range, where a wider porosity range is shown. No Z^*-value is obtained for the grain size distribution of 125 - 150 μm, because the model only fits to porosities that are < 28%. These values are not obtained by the uniaxial experiments carried out on this grain size distribution. The values that are obtained from the experiments as shown in this report are consistent with the Z^*-values obtained by Spiers et al. (1990) (i.e. between$1.78 * 10^{-19}$ and $5.91 * 10^{-20}$ $m^3 s^{-1}$) as discussed. On the basis of mechanical data, the behavioral regime for 0.175 MPa < σ < 2.75 MPa and 50 μm $\leq$ d $\leq$ 150 μm shows diffusion controlled pressure solution for low volumetric strains ($e_v < 15\%$).

Table 6: *Values and parameters used in the pressure solution model presented by Spiers et al. (1990)*

Symbol	Definition	Value/range	Source and additional information
A	Grain shape and packing factor divided by gas constant	33	Spiers et al. (1990)
a	Numerical exponent	2	Spiers et al. (1990)
d	Grain size μm	50-90; 90-125	-
V_m	Molar volume of solid phase ($m^3 mol^{-1}$)	2.693×10^{-5}	Koelemeijer et al. (2012)
T	Temperature (K)	293.15	-
e_v	Volumetric strain	$5 - 10\%$ or $\frac{\phi_0 - \phi}{1-\phi}$ where $\phi_0 = 30\%$	Spiers et al. (1990)

6.1.2 Theoretical model - Pluymakers and Spiers (2014)

In this subsection, the model of Pluymakers and Spiers (2014) (model 3: equation (25)) is compared to the experimental data on compaction of granular salt to predict the evolution of compaction creep rate with progressively decreasing porosity (ϕ/ϕ_0) for granular salt. This model is basically the same as the model presented by Spiers et al. (1990), but expresses the strain/ϕ dependence differently. However, the model is not accurate for porosities smaller than $\sim$3% since the approximation made in this model for grain contact area A_c is no longer accurate.

The experimentally measured porosities (ϕ_0 and ϕ) are used to cast the experimental data in the form of log strain rate versus log porosity for the different grain size ranges (Fig. 19). However, the start porosity (ϕ_0) in this model is defined as the initial state where the developed grain contacts are negligible, which is not realistic. a start porosity for a simple cubic pack of spheres will be $\sim$47%. This value is quite high as start porosity. Therefore, the start porosity as obtained in the compaction experiments is taken (i.e $\phi_0 \sim 30\%$). The resulting comparison of the experimental data with the pressure solution theory ables us to test the applicability with the model presented by Pluymakers and Spiers (2014) and to calibrate the Z^* value as done in the in the previous subsection with the model of Spiers et al. (1990). The values used for the parameters appearing the the model are given in Table 7. A DS value for the grain size distribution of 50 - 90 μm of 5×10^{-18} is calibrated (Fig. 19). For the grain size distribution of 90 - 125 μm a DS value of 3×10^{-18} is calibrated. For this model also counts that the best fit is obtained for porosities $\sim$ < 28%. For porosities larger than $\sim$ 28%, the model is not accurate anymore, probably because this model assumes that there are no grain contacts at the moment of zero compaction (ϕ_0). From the microstructural observations we can see that grain contacts already developed. The DS values obtained by the model of Pluymakers and Spiers (2014) are one to two order of magnitude lower compared to the Z^* value obtained by Spiers et al. (1990). Both models assume spherical grains and therefore, the Z^* values obtained by both models are close to each other. For the grain size range d = 90 - 125 μm, the Z^* values obtained by the models differ with 2 order of magnitude, because the experimental data that is obtained by the compaction experiments and plotted in Figure 19b show only a porosity decrease of a few percentage. More data is needed for this grain size distribution to obtain a more accurate Z^* value for different porosities.

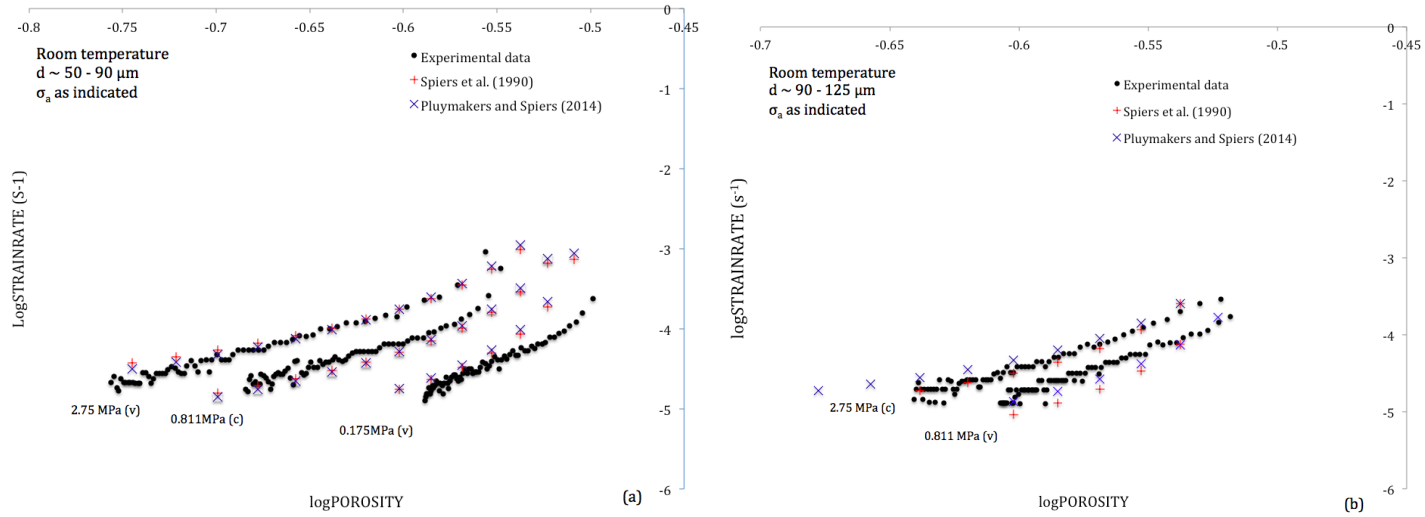

Figure 19: *LogPOROSITY versus logSTRAINRATE plots. The black dots represent the data obtained from the uniaxial experiments. The other symbols represent the calibrated data by the model of Spiers et al. (1990) and Pluymakers and Spiers (2014). (a) Plots for the grain size distribution of 50 - 90 µm. A stress of 0.811 MPa is used to calibrate (c) the Z^* value. The applied stresses of 2.75 MPa and 0.175 MPa are used to verify (v) the obtained Z^*-value. (b) Plots for the grain size distribution of 90 - 125 µm.*

Experimental data comparison with the model of Spiers et al. (1990) and Pluymakers and Spiers (2014) show that both diffusion controlled pressure solution creep models are applicable for the conducted experiments. Note that porosities obtained by these experiments show only a porosity range between $\sim$ 30% and 17%. More experimental data for lower porosities is needed to compare the models with. The model does not fit for porosities larger than $\sim$30%. This might be the case, because the models are multiplied by a factor of $\frac{5\phi}{2}$ to correct for smaller porosities. New plots need to be made with the constitutive equation as presented by Spiers et al. (1990) and Pluymakers and Spiers (2014) and compared to new data that include higher porosities. Another reason for the misfit for higher porosities is that the assumption that the grains are spherical does not count for higher porosities. This means that the geometry of the packing with a higher porosity cannot be described as a simple cubic pack of spherical grains. In the next subsection, a new pressure solution creep model is presented that assumes a geometry based on the microstructural observations.

Table 7: *Values and parameters used in the pressure solution model presented by Pluymakers and Spiers (2014)*

Symbol	Definition	Value/range	Source and additional information
α	Geometric factor	0.9	van Noort and Spiers (2009)
A	Geometric constant	4	Pluymakers and Spiers (2014); Simple cubic pack of grains
C_s	Solubility of NaCl (m^3m^{-3})	0.165	Koelemeijer et al. (2012)
DS	Diffusion coefficient D; fluid thickness S (m^3s^{-1})	10^{-19} to 10^{-20}	Range determined for diffusion controlled pressure solution in NaCl (e.g. Spiers et al. (1990); Pluymakers and Spiers (2014))
F	Grain shape factor	π	Value for simple cubic pack of grains (Pluymakers and Spiers (2014))
R	Gas constant ($Jmol^{-1}K^{-1}$)	8.314	Pluymakers and Spiers (2014)
Z	Coordination number	6	Value for simple cubic pack of grains (Pluymakers and Spiers (2014))
Ω	Molar volume of NaCl (m^3mol^{-1})	2.705683796×10^{-5}	Koelemeijer et al. (2012)

6.2 Densification versus pressure solution theory

6.2.1 Densification behavior - diffusion controlled pressure solution

Having shown that the diffusion controlled models seems capable for approximating experimental strain (up to ∼10%) in salt, the theoretical models of Spiers et al. (1990) and Pluymakers and Spiers (2014) are used to estimate the densification time under different conditions. Hereby we assume that diffusion controlled pressure solution is the only deformation controlling mechanism during densification. The models give an estimated healing time for a porosity decrease from the average start porosity (ϕ_0) of 30% to a final porosity (ϕ) of 5%. A final porosity of 5% is chosen, because (1) this value is in general considered as the percolation threshold for a porous medium and hence the porosity at which sealing should be complete (i.e. the point where all remaining porosity becomes disconnected) (Pluymakers and Spiers (2014)) and (2) the analytical model is not applicable for smaller porosities since the grains do not represent spherical but cubic grains from that point on. For the theoretical diffusion controlled pressure solution model of Spiers et al. (1990) the healing time is calculated by

$$\dot{\varepsilon} = N\frac{1}{e_v^2} \tag{43}$$

Where $N = AV_m\frac{Z^*}{T}\frac{\sigma_a}{d^3}$. e_v can be expressed as

$$e_v = e^{\varepsilon} - 1 \tag{44}$$

Equation43 is substituted intoo Equation44 to obtain a relation between strain rate and strain

$$\dot{\varepsilon} = N\frac{1}{(e^{\varepsilon}-1)^2} \tag{45}$$

and is integrated in order to provide a relation for strain against time

$$\int_0^{\varepsilon}(e^{\varepsilon}-1)^2 d\varepsilon = N\int_0^t dt \tag{46}$$

$$t = \frac{\varepsilon + 0.5e^{2\varepsilon} - 2e^{\varepsilon} + \frac{3}{2}}{n} \tag{47}$$

Where ε can be written as a function of porosity and substituted in equation47 by

$$\varepsilon = ln\left(1 + \left(\frac{\phi_0 - \phi}{1-\phi}\right)\right) \tag{48}$$

The model is applied to estimate the densification time for NaCl under in situ stress, pressure and temperature conditions as those employed in the uniaxial experiments. The time it takes to go from the initial porosity (ϕ_0) of 30% to final porosity (ϕ) of 5% for different applied stresses and grain sizes predicted by the model of Spiers et al. (1990) is shown in Figure 20. The initial porosity represents the porosity after the dry pre compaction. Using the parameter values in equation (34) as listed in Table 6 and varying the applied stress from 2.75 MPa to 0.175 MPa for grain size ranges of 50 - 90 μm and 90 - 125 μm, shows that the densification time decreases rapidly with increasing normal stress and decreasing grain size.

For comparison, the diffusive controlled compaction creep model of Pluymakers and Spiers (2014) is used to estimate the healing time (porosity from 30% to 5%) for the granular salt samples saturated with saturated NaCl solution. A relation between strain rate ($\dot{\varepsilon}$) and time (t) could be derived with a dependence on the assumed starting- and end porosity. A simplified equation of the diffusive controlled compaction creep model can be written as

$$\dot{\varepsilon} = M\left(\frac{2\phi_0}{2\phi_0 - 2\phi}\right)^2 \tag{49}$$

Where $M = \frac{4\pi A_d Z}{F}\frac{DCS}{d^3}\frac{\sigma\Omega}{RT}\frac{Z}{F}$. The strain ($\varepsilon$) needed to reduce the porosity from the initial porosity (ϕ_0) to the final porosity (ϕ) is given by the relation of strain against volumetric strain and can be written as

$$e_v = e^{\varepsilon} - 1 \tag{50}$$

The relationship of volumetric strain against porosity is given by

$$e_v = \frac{\phi_0 - \phi}{1-\phi} \tag{51}$$

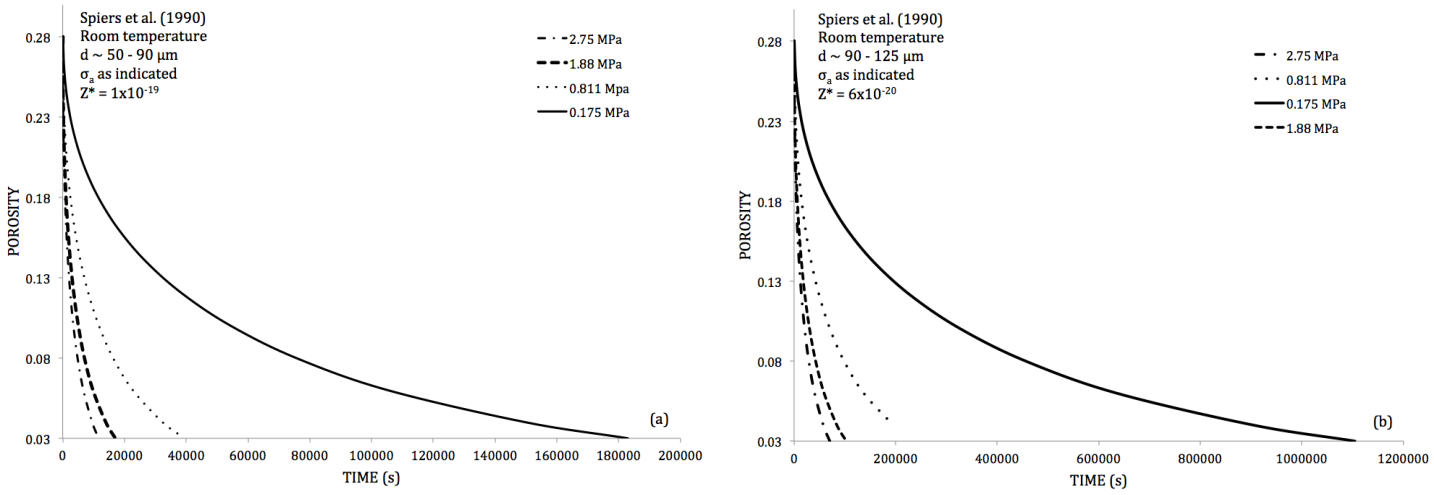

Figure 20: *Densification time of salt for a porosity decrease of 30% → 5% as predicted by the model of Spiers et al. (1990) for grain size ranges of (a) 50 - 90 µm and (b) 90 - 125 µm.*

By substituting equation (37) into equation (38) and rewriting the terms of porosity as a function of strain, gives the following relation of porosity against strain

$$\phi = \frac{e^{\varepsilon} - 1 - \phi_0}{e^{\varepsilon} - 2} \tag{52}$$

A relationship for strain rate ($\dot{\varepsilon}$) against strain (ε) can obtained by

$$\dot{\varepsilon} = \left(\frac{2\phi_0}{2\phi_0 - 2\left(\frac{e^{\varepsilon}-1-\phi_0}{e^{\varepsilon}-2}\right)} \right)^2 M \tag{53}$$

Equation (40) can be integrated in order to provide a relation for strain against time (equation (41) - equation (43))

$$M \int_0^{\varepsilon} \left(\frac{2\phi_0 - 2\left(\frac{e^{\varepsilon}-1-\phi_0}{e^{\varepsilon}-2}\right)}{2\phi_0} \right)^2 d\varepsilon = \int_0^t dt \tag{54}$$

$$\frac{\frac{1}{2}(\phi_0 - 1)\phi_0(\varepsilon + log(2 - e^{\varepsilon}))}{M} + constant = t \tag{55}$$

$$t = \frac{\frac{1}{2}(\phi_0 - 1)\phi_0(\varepsilon + log(2 - e^{\varepsilon}))}{M} \tag{56}$$

The model is applied to estimate the densification time for NaCl under in situ stress, pressure and temperature conditions as those employed in the uniaxial experiments. The initial porosity represents the porosity after the dry pre compaction. Using the parameter values in equation (31) listed in Table 7 and varying the applied stress from 2.75 MPa to 0.175 MPa for grain size ranges of 50 - 90 μm and 90 - 125 μm, shows that the healing time decreases rapidly with increasing normal stress and decreasing grain size. The results obtained by the compaction experiments are plotted in the time versus porosity graphs and compared to the healing model (Fig. 21). The healing model based on the diffusive controlled pressure solution model is compared with the healing model of Spiers et al. (1990). The healing model based on Pluymakers and Spiers (2014) shows a longer densification time, because the geometry of the grains are described different in both models. As mentioned earlier, these estimated healing times are only applicable when diffusion controlled pressure solution is the dominant deformation mechanism. The microstructural observations showed already necking features at higher strains, which suggest an approach to microstructural equilibrium at longer compaction times. The neck growth at higher volumetric strains indicate a transition from non-equilibrium pressure solution creep at lower strains to a neck-growth type of process at higher strains. Based on the long term controlled compaction experiments shown in the next subsection, we will investigate whether of not other deformation processes takes over and when healing occurred.

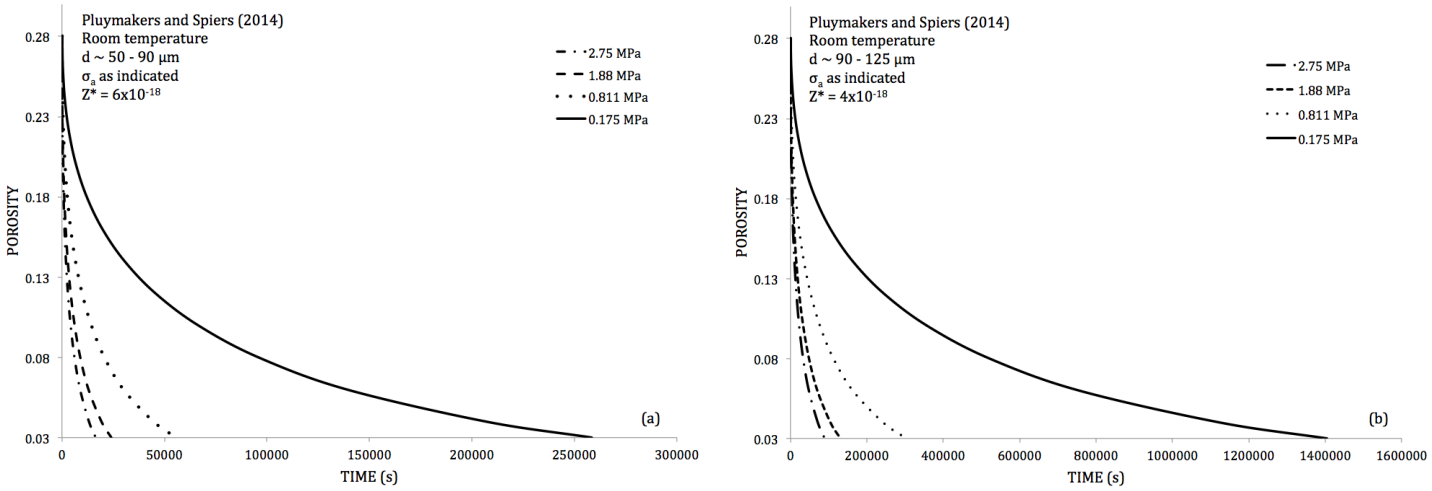

Figure 21: *Densification time of salt for a porosity decrease of 30% → 3% as predicted by the model of Pluymakers and Spiers (2014) for grain size ranges of (a) 50 - 90 µm and (b) 90 - 125 µm.*

6.2.2 Densification and Healing based on the long term experiments

We have proven that pressure solution creep was the dominant mechanisms for densification for low volumetric strains (i.e. up to ∼15%). By comparing the long term compaction experiments with the pressure solution model of Spiers et al. (1990), we see that at a strain of ∼20% (σ=1.08MPa; d=63-71μm) the experimental data does not follow the analytical data anymore (Fig. 22(Left)), suggesting that from this moment on other deformation mechanism(s) might become dominant.
The possible change is mechanism is also clear when plotting log_{10}strain versus log_{10}strain rate. The experimental data follows the analytical model and shows a slope with a value between 1 and 2, which is consistent with the diffusion controlled pressure solution model of Spiers et al. (1990). However, the slope becomes steeper at a strain of ∼20% and shows a value of ∼7. At a strain of ∼35% (ϕ∼24%) no compaction is observed anymore suggesting that healing occurred. Schutjens (1991) conducted long term compaction experiments where the grain size was changed and the applied stress was kept constant. The experiments showed that higher volumetric strains were reached for lower grain sizes and whereby healing occurred at higher volumetric strains and lower porosities for a smaller grain size. During the long term compaction experiments in this report, the grain size is kept constant while the applied stress is changed. Fig. 9 shows that another mechanism occurred at lower porosities (and therefore higher volumetric strains) when a higher stress is applied (constant grain size).
Visser et al. (2012) suggests that there is a possibility that peripheral neck growth processes that were driven by interfacial energy forces might become significant high at these strains, because of the increased contact area and associated contact stress. The driving forces for pressure solution creep and neck growth varies strongly and depends on parameters including e.g. grain size, stress and surface energy (γ). For grain boundaries that have an island channel structure, neck growth can occur as well, resulting in growth of the islands and hence grain boundary healing. Note that we define healing as increase in strength, hence increase in elastic stiffness. Experimental data obtained during the long term experiments (i.e.porosities down to ∼5%) showed indeed that the densification by pressure solution creep decelerates and stops. This happened when the driving force due to the applied stress approaches the driving force due to surface forces (Visser et al. (2012)). From this point on, contact healing will occur as the chemical potential of the dissolved solid in the pores reaches the solid potential within the grain boundary (van Noort et al. (2008); Visser et al. (2012)). Another explanation could be that the grain contact stress become low so that neck or island-growth processes will dominate over pressure solution creep.
To test whether healing occurred, the microstructural data was compared with a healing model. E.g., Visser (1999); van Noort et al. (2008) supposed a strain and grain size dependent 'yield stress' at which densification driven by pressure solution stops and is prevented by grain boundary healing. The model of van Noort et al. (2008) that predicts the stress conditions at which grain boundary healing is expected is given by

$$(\sigma_n - P_f) < \sigma_{crit} = 2\alpha\sqrt{E\frac{\gamma_{sl}}{\delta}\left(cos\frac{\theta}{2} - cos\frac{\theta_{eq}}{2}\right)} \tag{57}$$

This shows the mean effective normal stress (σ_n-P$_f$) for the compaction of a granular aggregate below which healing will dominate. Table 8 shows the definition and values of the parameters as used in 57 and 61. The critical stress (σ_{crit})

denotes the stress on the grain boundaries below which deformation by integranular pressure solution will not proceed (van Noort et al. (2008)). The critical stress was calculated according to the predictions of van Noort et al. (2008). The values used to calculate the critical stress were displayed in Table 8. According to the analytical model of van Noort et al. (2008), a critical effective contact stress in the range of 43 - 86 MPa was calculated.
For the experiments, the critical stress was estimated by using the contact area projected parallel to the area of the upper piston. Since this is the area that undergoes the external force. Correction were made for to measure only the area that undergoes the stress from the thick section. Note that vertical grain contact areas do not encounter as stress, while horizontal grain contact encounter the total stress and grain contacts oblique to the force encounter a stress in between. The force balance used to calculate the critical stress is given by

$$\sigma_e A_e = N_c \tilde{\sigma}_{crit} \bar{a}_c \tag{58}$$

This can be rewritten as

$$\sigma_e A_e = \tilde{\sigma}_{crit} A_c \tag{59}$$

Where σ_e presents the external stress (i.e. imposed stress during compaction), A_e the external area (i.e. area of the piston), $\tilde{\sigma}_{crit}$ the critical stress of the contact area, $\bar{a}_c$ the average contact area, N the amount of areas and A_c the total contact area. The critical stress derived from the microstructural observations can therefore be calculated by

$$\tilde{\sigma}_{crit} = \frac{A_e}{A_c} \times \sigma_e \tag{60}$$

Note that the contact area calculated from the thin sections were multiplied by a factor 4, because of the conversion to three dimensions. By assuming that the maximum line length represents the true contact diameter and the minimum line length is equal to zero (i.e. no grain contact), the average line length is about equal to half of the true contact diameter. By quadrating, because we want to know the area we will get a factor of 4. A critical stress of 55 MPa was found. This value is in the range as the predictions of van Noort et al. (2008) show. Based on this critical stress, we can assume that the mechanism of healing occurred at low porosities (and high volumetric strains (32%)).
Besides the critical stress, the critical porosity at which grain boundary healing occurred was calculated according to the predictions of van Noort et al. (2008). The critical porosity at which healing starts in calculated by

$$\phi_{crit} = 1 - \pi/3\sqrt{3} - 8/\pi\sigma_n/\sigma_{crit} \tag{61}$$

For salt healing, the predicted critical porosity has a value ranging between 34 and 36%, whereas the experimental data show a critical porosity of ∼20%. The critical porosity as obtained by the compaction experiments at which pressure solution stops and healing occurs, is below the predictions of van Noort et al. (2008). A reason for the differences in value could be that the input parameters used to predict the critical porosity were wrong, since these parameters can vary. The input parameters to calculate the critical stress are not constants. For example, the fluid film thickness can vary from 40 to 250nm. Also, Youngs Modulus can deviate depending on the grain boundary and hardening during compaction. Another reason might be that another mechanism is operating instead of healing and therefore does not fit to the predictions on van Noort et al. (2008).

Table 8: *Definitions, parameters and values as used in 57 and 61*

Parameter	Definition	Value	Unit
α	Total island area fraction	0.2 - 0.4	-
δ	Grain boundary width	50	nm
E	Young's modulus salt	30.0	GPa
γ_{sl}	Interfacial energy between the solid and the liquid phase (salt)	0.1133	Jm^{-2}
$cos\frac{\theta}{2} - cos\frac{\theta_{eq}}{2}$	Dihedral angle (θ); Equilibrium dihedral angle (θ_{eq})	0.17	-

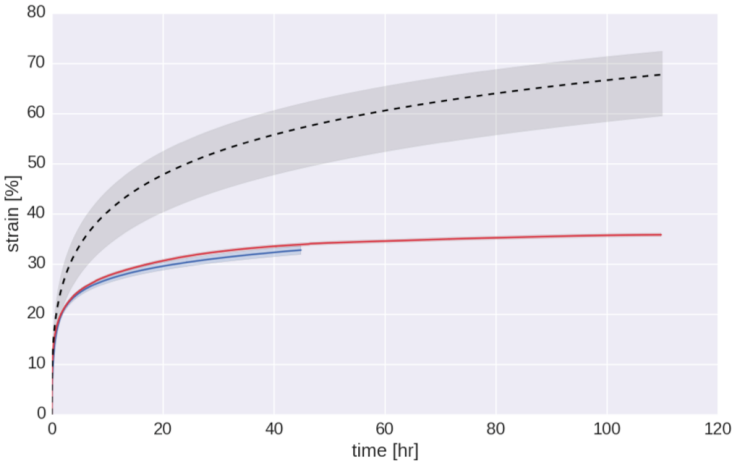

Figure 22: *Strain versus time. The red and blue lines show the experimental data. The black dotted line shows the analytical model of Spiers et al. (1990).*

6.3 Microstructural analysis

6.3.1 Microstructural interpretation

Based on the microstructural analysis, different deformation mechanisms were observed at low and high volumetric strains. First of all, the observed mechanical behavior as pressure solution creep was associated with grain-to-grain indentations, truncations and overgrowths that were observed in the microstructures. E.g., Spiers and Schutjens (1999); Urai and Spiers (2007) suggested that pressure solution creep was often associated with rearrangement of grains and grain boundary sliding. The combination of the mechanical data and the theoretical models of both Spiers et al. (1990) and Pluymakers and Spiers (2014) suggest that (diffusive) pressure solution creep was the dominant deformation mechanism at low volumetric strains (e_v<15%). Therefore, the results obtained by the comparison of the experimental results with the mentioned theoretical models were consistent with the microstructural observations. The observed pressure solution like structures as truncations and grain-to-grain indentations show that pressure solution controls the densification of brine saturated NaCl for volumetric strains ≤15%. The microstructures show that grain-to-grain indentations and truncations are observed at volumetric strains ≤6%. This makes clear that dissolution and precipitation of the material occurs at the begin stage of the compaction.
At higher volumetric strains (e_v>20%) necked grain contacts were observed in combination with pressure solution like structures. Pharr and Ashby (1983) suggest that the necked grain contacts were expected in dissolution-coupled creep mechanisms. Neck growth is exclusively driven by gradients in curvature and reduction in surface energy (Hickman and Evans (1991)). The grains are tending to weld together when the fluid wetting angle between the grains does not equals θ_{eq}. The observation of neck growth in the thin section might be a possible explanation that the compaction curve does not follow the pressure solution creep model anymore. The neck growth observed at higher volumetric strains (e_v>20%) indicates the transition from non-equilibrium pressure solution creep at lower strains to neck growth processes at higher strains (Visser et al. (2012)). For higher volumetric strains (>32%) only a few neck growth structures were observed. However, it might be possible that the porosity is too small to observe neck growth.
Another deformation mechanism that was observed in the microstructure representing high volumetric strains (exp.21) was grain boundary migration, as indicated by concave and convex grain boundaries. E.g., Schenk and Urai (2004); Urai and Spiers (2007) suggest that fluid assisted grain boundary migration (fluid present in the form of saturated brine inclusions or grain boundary films), reduces the dislocation density and hence the stored energy of dislocations. The process of grain boundary migration was driven by chemical potential differences across grain boundaries (Urai and Spiers (2007)). These potential differences were related to differences in dislocation density between old grains that were already deformed and new grains (Peach et al. (2001); Urai and Spiers (2007)).

6.3.2 Grain contact and pore wall area

An estimation on the grain contact area and pore wall area for the experimental data was made based on image analyses and compared with the analytical pressure solution models of Spiers et al. (1990) and Pluymakers and Spiers (2014). The samples that were analyzed are presented in Tabel 5 and 9. The mean contact area per grain for the analytical models was calculated by

$$A_c = Fd^2 f(\phi) \tag{62}$$

where Table 10 shows the parameters and values as used for the analytical models to predict the evolution of grain contact with decreasing porosity. Equation(62) predicts that the contact area increases with decreasing porosity. For comparison with the data provided by the thin sections, corrections were made because of the different dimensions. The thin sections represent two-dimensional images, while the analytical models are applicable for three-dimensional images. The conversion of a two-dimensional size distribution to a three dimensional size distribution is a complex problem (e.g. Higgins (1994); Kumara et al. (2012)). The main problem include the cut effect that the intersection plan does not pass directly through the center of the grain, parallel to the longest axis (Higgins (1994)) and assumptions that has to be made to estimate the three-dimensional grain shape. To solve this problem, we assume spherical grains with circular grain contacts since this is the closest to the geometries assumed in the analytical models. The contact area (A_c) was calculated from the two-dimensional images by assuming the line length provided by Jmicrovision as the diameter of the grain contact area. The contact area, however, as calculated from the thin sections is multiplied by factor 4 to correct for the different dimensions. A factor 4 was taken, because we assume that the maximum line length represents the true contact diameter and the minimum line length is equal to zero (i.e. no grain contact), meaning that the average line length equals half of the true line length. The average grain contact area per grain was calculated by

$$A_c = \frac{\Sigma((\pi(0.5d)^2) \times 4)}{N_2} \tag{63}$$

Where d denotes the line length as measured from the thin section and N_2 the amount of grains whereby grain contacts were detected. Figure 23 shows that the total grain contact increases with decreasing porosity. The experimental data follows the experimental data for pressure solution.
The grain contact area per grain (A_c) was calculated by dividing the total contact area of the grain (by using total line length (l_c) by the total amount of grains. Figure 23 shows the change in grain contact area with decreasing porosity for both experimental data and analytical models.
The pore wall area was calculated for the analytical models by

$$A_{pw} = A_{tot} - A_c \tag{64}$$

Where A_{tot} represents the total area of the grain. For the experimental data, A_{tot} was calculated by using the average grain size as measured during image analyses. The average equivalent circular diameter is chosen as representative grain size.
Figure 23 shows the change in pore wall area with decreasing porosity for both experimental data and the analytical models. van Noort et al. (2008) suggest that pressure solution operates when the total surface of the contacts < area of the pore wall. For the plotted areas representing samples with low volumetric strains (e_v<10%) in Fig. 23. the total surface of the contacts is indeed smaller than the total pore wall area (Table 9). However, for the sample representing higher volumetric strains and a porosity of ∼20%, the the total area of the contacts > the total area of the pore wall. The change in contact area might stop pressure solution creep, since the increase in contact area will lower the stress applied on the grain contacts and therefore slow down or eventually stop pressure solution creep.

Table 9: *Contact-, pore wall- and total area at different porosities*

Name	Volumetric strain (%)	Porosity (%)	Contact area (m^2)	Pore wall area (m^2)	Total area (m^2)
Sample 1	0	45.47	$1.697e^{-09}$	$2.334e^{-08}$	$2.521e^{-08}$
Sample 2	6	37.4	$5.928e^{-09}$	$1.669e^{-08}$	$2.262e^{-08}$
Sample 3	9	30.94	$4.907e^{-09}$	$2.108e^{-08}$	$2.598e^{-08}$
exp.21	32	19.97	$6.426e^{-09}$	$8.014e^{-10}$	$7.238e^{-09}$

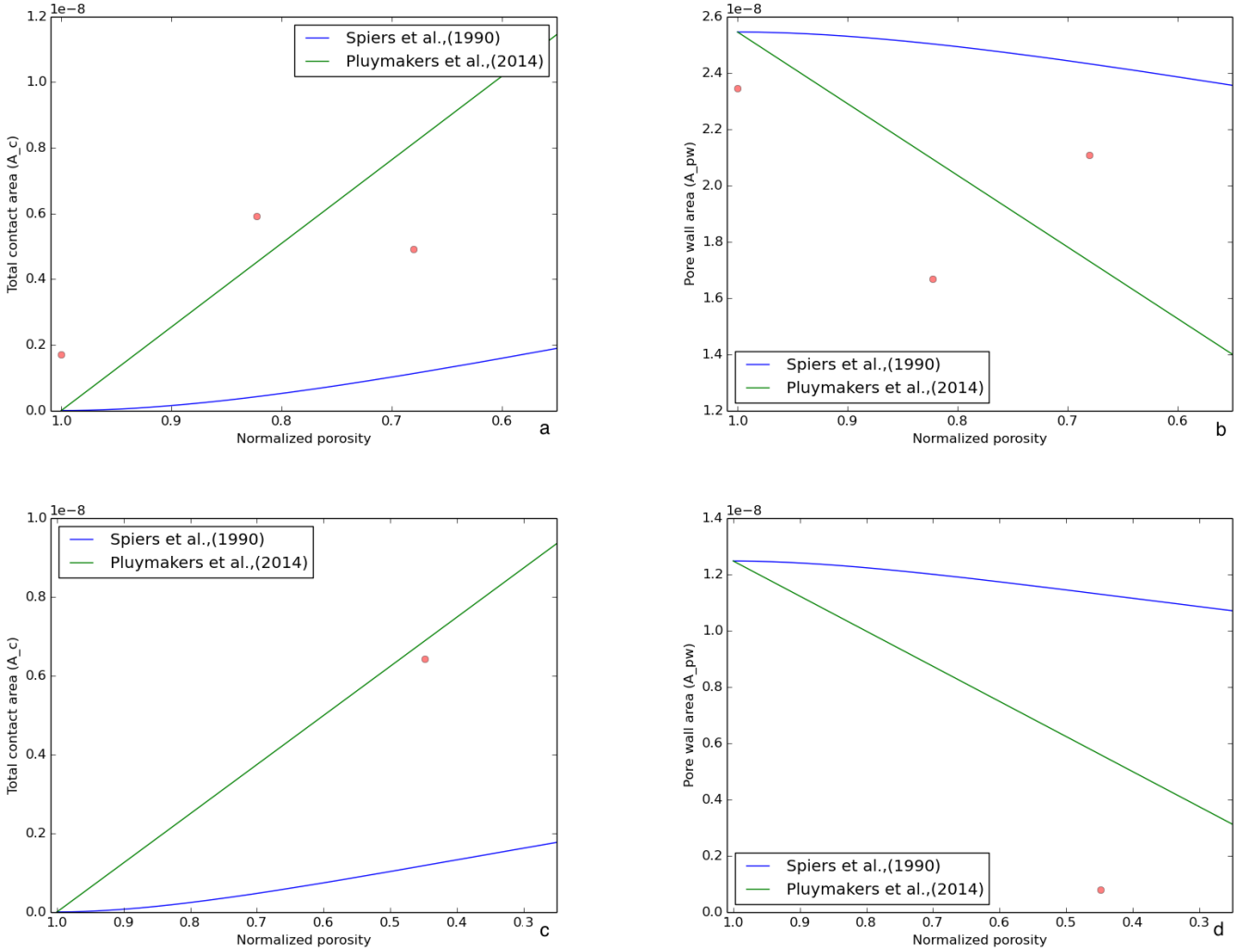

Figure 23: *Total grain contact area and pore wall area per grain plotted for the experimental data and analytical models against the normalized porosity. a. Total contact area low volumetric strains (e_v=0, 6 and 9%); b. Pore wall area low volumetric strains (e_v=0, 6 and 9%) and analytical models; c. Total contact area for high volumetric strain (e_v=32%); d. Pore wall area for high volumetric strain (e_v=32%)*

Table 10: *Function of porosities assumed by different authors for a simple cubic pack of spherical grains*

Parameter	Unit	Value	Equation/ Symbol	Source
Model Spiers et al. (1990)				
$f(\phi)$	-	-	$\frac{\phi_0-\phi}{1-\phi}$	Spiers et al. (1990)
Model Pluymakers and Spiers (2014)				
$f(\phi)$	-	-	$\frac{2\phi_0-2\phi}{2\phi_0}$	Pluymakers and Spiers (2014)
General - Sample 1,2,3				
Initial porosity	-	45.47	ϕ_0	Derived from experiments
Grain size	μm	90	d	Min. sieved grain size
Grain shape Factor	-	π	F	Spiers et al. (1990)
General - exp.21				
Initial porosity	-	44.60	ϕ_0	Measured during experiment
Grain size	μm	63	d	Min. sieved grain size
Grain shape factor	-	π	F	Spiers et al. (1990)

7 Recommendations

7.1 Improvements experimental set up and procedure

During the first dry and wet uniaxial compaction experiments conducted in Utrecht, sample grain size fractions of 50-105 μm were used. The mechanical results obtained by these experiments show barely reproducible compaction creep curves and are therefore excluded from the results. A possible explanation for this is that the grain size fraction turned out to be a too wide to obtain consistent results. The wide grain size distribution can vary the start porosity, because different grain sizes might be dominant in the different samples and give other compaction results. The diffusion models from e.g. Spiers et al. (1990) and Pluymakers and Spiers (2014) show that diffusion controlled pressure solution creep is strongly dependent on grain size (i.e. d^3). In the following experiments the grain size distribution is minimized to make better predictions on the influence of the grain size (i.e. 150-125, 90-125, 50-90 μm). The sample grain size fractions of 50-105 μm were dry pre compaction for 10 minutes. According to Zhang and Spiers (2005) the dry pre compaction time is increased up to 30 minutes for the experiments with a smaller grain size fraction to achieve a start porosity of ∼30% and minimize the differences in packing to avoid an initial jump at the starting point of wet compaction. The position of the brass base with respect to the weight varies per experiment. To correct for this, a plastic Uniaxial Salt Deformation Apparatus (USDA) is developed to align the brass base and the weight (Fig. 4). The pistons that are used for the sample grain size fractions of 50 - 105 μm deformed easy. Stronger pistons are developed that fit perfectly in the capillary tube and therefore minimize the effect of friction between the piston and the capillary tube, because the straight and better fit pistons avoid the granular salt to come upwards in the capillary tube to surround the piston. As well, the better fit of the new upper piston avoid the fluid to leak into the sample at the moment that the fluid is placed in the fluid reservoir, before the fluid is sucked through the sample. Another solution to minimize the frictional effects at the piston/tube surface is to place a filter paper with a diameter of 1 or 2 mm between the sample and the piston to avoid the grains to come upwards or attach graphite on the walls of the capillary tube. No grain size larger than 150 μm was used, because of the frictional effects at the sample/tube surfaces. For the results in this report, we assume that the applied loads are high enough and the grain size small enough to avoid significant errors caused by the frictional effects at the piston/tube and sample/tube surfaces. Visser et al. (2012) apply friction determinations to quantify the frictional effects at the piston/tube and sample/tube surfaces by measuring only the force that is applied by the inner column (consisting of the lower piston, sample and upper piston) by the balance. The spring in the dial gauge used for all the experiments supplies a load of ∼60 gram. To minimize the applied load of the spring in the dial gauge meter on the sample, the linear spring is removed from the dial gauge meter. The dial gauge without spring was placed in a clamp stand and positioned over a balance. The dial gauge was clamped in such a way that the balance measured only the weight applied by the dial gauge meter at a certain displacement. The calibration of the dial gauge before and after removing the spring is illustrated in Figure 24. The load that is applied by the dial gauge meter after removal of the spring is ∼20 grams. For the long term experiments conducted in this report, gap sensors are used for more accurate measurements. As well, the porosity as calculated in the short term experiments is underestimated. The method of calculating the porosity for the long term compaction experiments is more accurate. To account for friction effects while conducting the long term compaction experiments, a circular paper is placed between the upper piston and the sample to obviate grains between the upper piston and the glass tube. Also, the sides of the glass

tube coated with graphite powder.

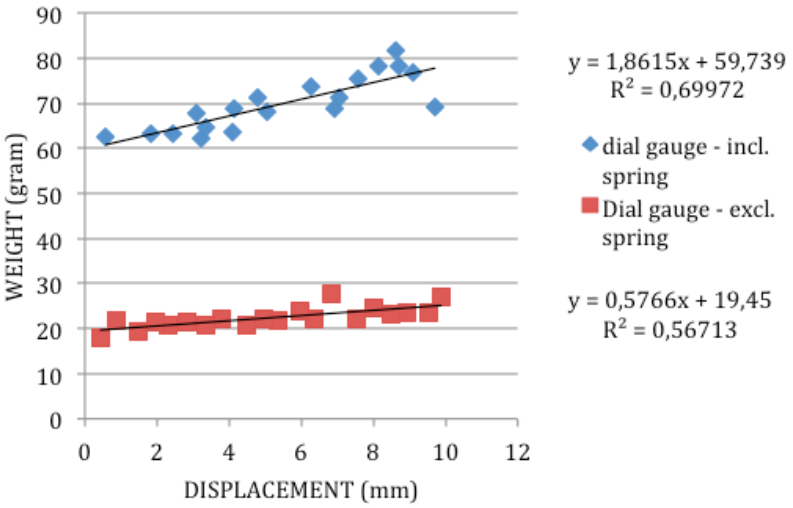

Figure 24: *Calibration of dial gauge meter. The blue dots indicate the calibration of the dial gauge meter including the linear spring. The red dots indicate the calibration of the dial gauge meter excluding the spring.*

7.2 Improvements microstructural methods

When removing the samples out of the capillary tube, one has to make sure that the samples are pushed directly on a flat glass plate otherwise the sample tends to break. Fold a tray made of tinfoil around the glass plate to avoid that the sample rolls from the glass plate during transport. Also, impregnate the sample with epoxy when the sample is located in a folded tinfoil tray (without the glass plate). Make sure that the tray does not leak. To make high quality thin sections it is important to position the impregnated sample in the vacuum chamber for at least 15 minutes and no longer than ∼30 minutes, because the ratio of the components that forms the epoxy might change. A lot of air bubbles will be present if the quality of the vacuum chamber is not high enough. It is also important to rinse the sample and the holder regularly, because new scratches are easily made. The best improvement to get a high quality image is by covering the sample with a cover slip. Glycerin is used to attach the cover slip on the sample and will fill the remaining scratches. Remove the glycerin from the thin sections when preserving the thin sections in a low humidity room. Presumably, the glycerin allows salt grains to dissolve even when the thin sections are stored in a low humidity room. Image analysis programs as e.g. ImageJ need contrast between the pores and the salt grains to analyze the image. We tried to achieve this contrast by 1. Coat the thin section with gold. After coating the thin section with gold, the coating was wiped away easily. 2. Dissolve NaCl and replace it for PbCl. By doing this, NaCl was indeed covered by PbCl, but it happened that the PbCl precipitated on top and the sides of the grains and on top of the epoxy. When cleaning it with saturated NaCl solution, the PbCl was slightly removed from both the grains as the pores. After 3 days, not even all the grains where colored black, but the thin section seemed to be in a new equilibrium. We could not dissolve any grain by trying to dissolve NaCl out of the thin section. 3. Dissolve all the salt grains from the thin section and fill it with graphite solution. When removing the graphite from the epoxy, by sandpapering the thin section dry (polish it dry did not work), new scratches were made in the thin section, which showed pictures of poor quality. We could not polish the section with e.g. diamond polish, because this removed the graphite. Non of the above methods give the result as needed for image analysis. A better option to tackle the problem is to impregnate the sample with colored epoxy.

8 Further research

Further research need to be done on image analysis. More data is needed to give more accurate predictions of pore wall area and grain contact area. Also, calculations on surface energy variations need to be made. Additional experiments on brine saturated granular salt can be conducted for higher volumetric strains (i.e. $e_v > 15\%$) to investigate which mechanism will be dominant at higher strain rates and drives the healing. Further modeling work is needed to derive closed formulations that allow predicting the change of microstructure and poromechanical properties of rocks upon time-dependent damage and healing. Also, numerical tools need to be developed for coupled simulations that involve thermo-hydro-chemo-mechanical damage and healing processes.

9 Conclusions

1. Rapid creep occurred during uniaxial compaction of NaCl in the presence of saturated brine solution and was primarily due to diffusion controlled pressure solution creep. An increase in compaction creep was promoted by an increased applied stress and a decrease in grain size, confirming the diffusion controlled pressure solution models at low volumetric strains (<15%) (i.e. high porosities).
2. At high volumetric strains (>20%) the diffusion controlled pressure solution models overestimated the creep rate and does not fit the experimental data. At volumetric strains of 32%, no creep was observed, whereby d=63-71μm and σ=1.08MPa.
3. Microstructural analysis confirmed the pressure solution creep as dominant deformation mechanism at low strains. Overgrowths, indentations and truncations were observed. Neck growth was observed at volumetric strains >15%, indicating that the systems goes to equilibrium at longer compaction times and interfacial energy forces became significant, because of the increased grain contact and lower contact stresses. At volumetric strains >32% no creep was observed anymore and besides some neck growth, grain boundary migration and formation of new grains were observed.
4. At low strains, the grain contact area < pore wall area and pressure solution creep was the dominant mechanism. At high strains (>32%), however, the grain contact area > pore wall area and pressure solution creep eventually stopped.
5. A yield stress, when grain boundaries heal and pressure solution creep stops, of 55 MPa was found at a volumetric strain of 32%, confirming the critical stress as predicted by healing models. The deformation mechanism observed when healing occurred were grain boundary migration and neck growth. Since neck growth was observed, it could be the possible mechanism that controls the contact healing. However, more research on surface energy and microstructures need to be done to investigate the details of the mechanism that controls healing.

10 Acknowledgements

First of all, I would like to thank Dr. Prof. C.J. Spiers and Dr. C.F. Arson who guided me through the research. They were both really enthusiastic about the research and supported me fully during my stay at Georgia Institute of Technology. Eimert de Graaff and Peter van Krieken are thanked for the technical assistance. Cheng Zhu deserves my special thanks for the extra guidance I needed throughout the research during my stay at Georgia Institute of Technology and afterwards. Finally, I would like to thank Martijn van den Ende for the collaboration on the long term compaction experiments and extra guidance I needed for the image analysis.

11 References

Chen, D., B. Weiss, and R. Stickler (1996). A model for crack closure. *Engineering Fracture Mechanics 53*(4), 493–509.

Hickman, S. H. and B. Evans (1991). Experimental pressure solution in halite: the effect of grain/interphase boundary structure. *Journal of the Geological Society 148*(3), 549–560.

Higgins, M. D. (1994). Numerical modeling of crystal shapes in thin sections: estimation of crystal habit and true size. *American Mineralogist 79*, 113–119.

Houben, M., A. ten Hove, C. Peach, and C. Spiers (2013). Crack healing in rocksalt via diffusion in adsorbed aqueous films: Microphysical modelling versus experiments. *Physics and Chemistry of the Earth, Parts A/B/C 64*, 95–104.

Koelemeijer, P. J., C. J. Peach, and C. J. Spiers (2012). Surface diffusivity of cleaved nacl crystals as a function of humidity: Impedance spectroscopy measurements and implications for crack healing in rock salt. *Journal of Geophysical Research: Solid Earth (1978–2012) 117*(B1).

Kumara, G., K. Hayano, and K. Ogiwara (2012). Image analysis techniques on evaluation of particle size distribution of gravel. *Int. J. Geomate 3*(1), 290–297.

Lehner, F. K. (1995). A model for intergranular pressure solution in open systems. *Tectonophysics 245*(3), 153–170.

Meer, S. and C. J. Spiers (1997). Uniaxial compaction creep of wet gypsum aggregates. *Journal of Geophysical Research: Solid Earth (1978–2012) 102*(B1), 875–891.

Peach, C., C. Spiers, and P. Trimby (2001). Effect of confining pressure on dilatation, recrystallization, and flow of rock salt at 150 c. *Journal of Geophysical Research: Solid Earth (1978–2012) 106*(B7), 13315–13328.

Pharr, G. and M. Ashby (1983). On creep enhanced by a liquid phase. *Acta Metallurgica 31*(1), 129–138.

Pluymakers, A. and C. Spiers (2014). Compaction creep of simulated anhydrite fault gouge by pressure solution: theory v. experiments and implications for fault sealing. *Geological Society, London, Special Publications 409*, SP409–6.

Popp, T., W. Minkley, K. Salzer, and O. Schulze (2012). Gas transport properties of rock salt–synoptic view. *Mechanical behavior of salt 7*, 143–154.

Raj, R. (1982). Creep in polycrystalline aggregates by matter transport through a liquid phase. *Journal of Geophysical Research: Solid Earth (1978–2012) 87*(B6), 4731–4739.

Rutter, E. (1983). Pressure solution in nature, theory and experiment. *Journal of the Geological Society 140*(5), 725–740.

Rutter, E. and D. Elliott (1976). The kinetics of rock deformation by pressure solution [and discussion]. *Philosophical Transactions of the Royal Society of London A: Mathematical, Physical and Engineering Sciences 283*(1312), 203–219.

Schaap, M. (1993, August). Intergranular pressure solution. Master's thesis.

Schenk, O. and J. L. Urai (2004). Microstructural evolution and grain boundary structure during static recrystallization in synthetic polycrystals of sodium chloride containing saturated brine. *Contributions to Mineralogy and Petrology 146*(6), 671–682.

Schutjens, P. M. T. M. (1991). Intergranular pressure solution in halite aggregates and quartz sands: an experimental investigation. *Geologica Ultraiectina 76*, 1–233.

Shimizu, I. (1995). Kinetics of pressure solution creep in quartz: theoretical considerations. *Tectonophysics 245*(3), 121–134.

Spiers, C., S. De Meer, A. Niemeijer, and X. Zhang (2003). Kinetics of rock deformation by pressure solution and the role of thin aqueous films. *Frontiers Science Series*, 129–158.

Spiers, C. and P. Schutjens (1999). Intergranular pressure solution in nacl: Grain-to-grain contact experiments under the optical microscope. *Oil & Gas Science and Technology 54*(6), 729–750.

Spiers, C., P. Schutjens, R. Brzesowsky, C. Peach, J. Liezenberg, and H. Zwart (1990). Experimental determination of constitutive parameters governing creep of rocksalt by pressure solution. *Geological Society, London, Special Publications 54*(1), 215–227.

Ter Heege, J., J. De Bresser, and C. Spiers (2005). Rheological behaviour of synthetic rocksalt: the interplay between water, dynamic recrystallization and deformation mechanisms. *Journal of Structural Geology 27*(6), 948–963.

Urai, J. and C. Spiers (2007). The effect of grain boundary water on deformation mechanisms and rheology of rocksalt during long-term deformation. In *Proc. 6th Conf. Mech. Beh. of Salt*, pp. 149–158.

van Noort, R. and C. J. Spiers (2009). Kinetic effects of microscale plasticity at grain boundaries during pressure solution. *Journal of Geophysical Research: Solid Earth (1978–2012) 114*(B3).

van Noort, R., H. J. Visser, and C. J. Spiers (2008). Influence of grain boundary structure on dissolution controlled pressure solution and retarding effects of grain boundary healing. *Journal of Geophysical Research: Solid Earth (1978–2012) 113*(B3).

Visser, H., C. Spiers, and S. Hangx (2012). Effects of interfacial energy on compaction creep by intergranular pressure solution: Theory versus experiments on a rock analog (nano3). *Journal of Geophysical Research: Solid Earth (1978–2012) 117*(B11).

Visser, H. J. M. (1999). *Mass transfer processes in crystalline aggregates containing a fluid phase*, Volume 174. Utrecht University.

Zhang, X., J. Salemans, C. Peach, and C. Spiers (2002). Compaction experiments on wet calcite powder at room temperature: Evidence for operation of intergranular pressure solution. *Geological Society, London, Special Publications 200*(1), 29–39.

Zhang, X. and C. Spiers (2005). Compaction of granular calcite by pressure solution at room temperature and effects of pore fluid chemistry. *International Journal of Rock Mechanics and Mining Sciences 42*(7), 950–960.

Zhu, C. and C. Arson (2014a). A model of damage and healing coupling halite thermo-mechanical behavior to microstructure evolution. *Geotechnical and Geological Engineering*, 1–22.

Zhu, C. and C. Arson (2014b). A thermo-mechanical damage model for rock stiffness during anisotropic crack opening and closure. *Acta Geotechnica 9*(5), 847–867.